

An abrupt switch in magmatic plumbing taps porphyry copper deposit-forming magmas

Lawrence Carter (✉ l.c.carter@exeter.ac.uk)

University of Exeter <https://orcid.org/0000-0003-3083-2361>

Simon Tapster

Geochronology and Tracers Facility, British Geological Survey <https://orcid.org/0000-0001-9049-0485>

Ben Williamson

Camborne School of Mines, University of Exeter <https://orcid.org/0000-0002-2639-3725>

Yannick Buret

Natural History Museum

David Selby

University of Durham

Ian Millar

British Geological Survey <https://orcid.org/0000-0002-9117-7025>

Daniel Parvaz

Lightning Machines <https://orcid.org/0000-0001-7690-7854>

Article

Keywords: magma, porphyry-type deposits, porphyry copper

Posted Date: June 24th, 2021

DOI: <https://doi.org/10.21203/rs.3.rs-608569/v1>

License:   This work is licensed under a Creative Commons Attribution 4.0 International License.

[Read Full License](#)

1 An abrupt switch in magmatic plumbing taps porphyry copper
2 deposit-forming magmas

3

4 Lawrence C. Carter^{1*}, Simon R. Tapster², Ben J. Williamson^{1,3}, Yannick Buret³, David Selby^{4,5}, Ian Miller² &
5 Daniel B. Parvaz^{6,7}

6

7 ¹Camborne School of Mines, University of Exeter, Cornwall, TR10 9FE, UK

8 ²Geochronology and Tracers Facility, British Geological Survey, Keyworth, Nottingham, NG12 5GG, UK

9 ³Natural History Museum, Cromwell Road, London, SW7 5BD, UK

10 ⁴Department of Earth Sciences, Durham University, DH1 3LE, UK

11 ⁵State Key Laboratory of Geological Processes and Mineral Resources, School of Earth Resources, China
12 University of Geosciences, Wuhan, 430074 Hubei, China

13 ⁶Selfrag AG, Biberenzelgli 18, 3210 Kerzers, Switzerland

14 ⁷Lightning Machines, 2nd Floor, Grove House, 774-780 Wilmslow Road, Didsbury, Greater Manchester
15 M20 2DR, UK

16

17 **Corresponding author. l.c.carter@exeter.ac.uk*

18

19 **Abstract**

20 Porphyry-type deposits are a vital source of green technology metals such as copper and molybdenum. They
21 typically form in subduction-related settings from large, long-lived magmatic systems. The most widely
22 accepted model for their formation requires that mantle-derived magmas undergo a multi-million year
23 timescale ramp-up in volatiles and ore-forming constituents in mid- to lower-crustal reservoirs, however this
24 does not explain why porphyry deposits are absent from the vast majority of arc magmatic systems. To
25 address this, we have carried out geochemical and geochronological studies on the tilted, ~8 km depth
26 equivalent, cross-section through the classic Yerington magmatic system, Nevada. Here we show that the
27 magmas underwent a major and abrupt change in chemistry over a period of 100 kyrs which is coincident
28 with the initiation of ore formation. This is attributed to a wholesale switch in the magmatic plumbing system
29 whereby volatile-rich granitic melts were extracted from an estimated ~30 km depth and transported to
30 shallow levels (~3-8 km) where exsolving fluids were focussed through highly permeable pathways to form
31 porphyry deposits. The change in magma chemistry is documented across the entire plutonic to volcanic
32 record. Its rapidity suggests that the increase in a magma's ore-forming potential is not solely driven by
33 tectonic factors, that occur over multi-million year scales, but through internal processes within the melt
34 evolution zone, operating at more than an order of magnitude faster than previously envisaged. This short
35 timescale narrows the temporal-geochemical footprint of magmas associated with porphyry mineralisation
36 which will aid in targeting the next generation of ore deposits.

37

38 Introduction

39 The shift to new and green technologies is driving the increasing requirement for metals^{1,2}. Copper demand
40 is forecast to increase by 140-350% from 2010 to 2050^{3,4}. Porphyry-type deposits provide more than 70% of
41 global copper, around 95% of molybdenum (~95%) and important amounts of gold (20%) and other metals⁵.
42 They form from hydrothermal fluids produced by large and long-lived calc-alkaline to slightly alkaline, water-
43 rich and relatively oxidising trans-crustal magmatic systems, mostly in subduction-related settings^{e.g.5-9}. Whilst
44 such magmas are arguably relatively common, porphyry-, and particularly large porphyry-type deposits are
45 extremely rare and increasingly difficult to find⁷. Their formation probably requires a series of specific
46 conditions and events during the evolution of the magmatic-hydrothermal system.

47

48 In the drive to discover new ore-deposits, there have been many recent attempts to develop whole-rock and
49 mineral geochemical indicators to assess the ore-forming potential, or the fertility, of magmatic systems¹⁰.
50 Their main advantage compared with conventional exploration techniques is that they are cheap and have
51 low environmental impact. Most indicators reflect the geochemical signatures of amphibole fractionation and
52 plagioclase suppression due to the hydrous nature of the magmas from which porphyry-type deposits
53 form^{e.g.7,11-20}.

54

55 The current paradigm is that the hydrous magmas that form porphyry-deposits result from an extremely long
56 (multi-million year), arc-scale, tectonically driven “ramp-up” in volatiles and ore-forming constituents in mid-
57 to lower-crustal magmatic reservoirs^{11,16,21-25}. Here, mantle-derived melts develop their hydrous ore-forming
58 geochemical signatures over protracted time scales due to cyclical fractionation and re-fertilisation by mafic
59 magmas, before emplacement into the upper crust. The macro-scale tectonic regime has been suggested to
60 progressively deepen the melt evolution zone and slow the upwards migration of magmas through the
61 crust^{22,24,26}. In an alternative model, it is suggested that magmas acquire their ore-forming geochemical
62 signatures during evolution within an upper crustal staging ground^{e.g.5,27,28}. Such conceptual models for the
63 evolution of magmatic systems linked to porphyry-style mineralisation are however greatly limited by a
64 paucity of vertically extensive exposure over the crustal windows of porphyry ore-forming systems²⁹. We
65 therefore have a fragmented understanding of the timescales of porphyry-deposit formation and the 4-D
66 architecture of the systems which produce them, which has hampered the development of genetic models
67 and exploration tools.

68

69 The Yerington magmatic system, Nevada, due to its unique ~8 km deep profile, from volcanic to plutonic
70 environments, through at least four porphyry copper deposits (Fig. 1 & 2) has provided constraints for many
71 of the most trusted porphyry system models^{e.g.5,6,27-32}.

72

73 Here we reconstruct the Yerington magmatic system across the deep plutonic to volcanic environment,
74 encompassing deep-seated melt evolution zones, through to the development and focusing of magmatic-
75 hydrothermal fluids to form porphyry-type deposits. In doing so, we examine the fundamental timescales and
76 drivers for the emergence of the magmatic system's ore-forming potential and associated geochemical
77 signatures that can be identified within the rock record.

78

79 The construction of a porphyry-forming magmatic system

80 Late Cenozoic basin and range extensional faulting and associated fault block rotation has exposed a <1 to
81 ~8 km palaeodepth cross-section through the middle Jurassic composite Yerington batholith^{27,33-36} (Fig. 1 &
82 2). There are three main plutonic phases, which listed in order of increasing emplacement depth are: 1) the
83 McLeod Hill quartz monzodiorite (McLeod QMD); 2) Bear quartz monzonite (Bear QM); and 3) Luhr Hill
84 granite (LHG) (Dilles, 1987). Swarms of granite-composition porphyry and aplite dykes cross-cut these,
85 appearing to be structurally focused through apophyses of the LHG^{27,32}. These dykes are spatially associated
86 with the batholith's four known porphyry copper deposits: Ann Mason; Yerington; MacArthur and Bear (Fig.
87 1 & 2). Combined, these host a resource in excess of 9 Mt of contained Cu^{35,37-39}.

88
89 The Yerington batholith was emplaced into Triassic to Jurassic intermediate composition volcanics,
90 volcanoclastic and argillaceous sedimentary rocks, and basal exposures of the Jurassic Artesia Lake
91 Volcanics, which are unconformably overlain by the Jurassic latitic Fulstone Spring Volcanics^{27,34,40} (Fig. 1 &
92 2). Units of the Fulstone Volcanics are thought to have been cogenetic with granite porphyry dykes
93 associated with the Luhr Hill granite^{40,41} or rather have been cogenetic with the nearby younger Shamrock
94 batholith and post-date porphyry mineralisation³⁴.

95

96 Temporal constraints from field relations

97 Field-based observations place constraints on the relative timing of events. The LHG is the youngest of the
98 three main plutons having been emplaced into the McLeod QMD and Bear QM²⁷. Contacts between the LHG
99 and McLeod QMD are sharp (Fig. S1), with no chilled margins or evidence of interaction with precursor
100 granitoids. No metasomatic effects are present at the contacts beyond the later, pervasive, mostly sodic-
101 calcic and propylitic porphyry-related alteration⁴². In deeper portions of the LHG (~7.5 km palaeo-depth²⁷),
102 banding defined by grain size variations is locally observed (Fig. S2).

103

104 The onset of porphyry mineralisation is constrained by cross-cutting relationships; multiple generations of
105 variably mineralised granite-composition porphyry and aplite dykes clearly cross-cut the upper (Fig. 3 & S3)
106 and lower parts of the LHG^{32,40} and appear to have been focused through apophyses of the LHG^{41,42}. The
107 dykes generally have sharp contacts with the LHG, with some showing chilled margins and others lobate
108 contacts (Fig. 3a). It was previously suggested that both the porphyry and aplite dykes emanated from
109 cupolas and upper zones (~3 to 6 km depth) of the LHG²⁷, however we could not trace either to their source
110 and therefore suggest that they were likely to be intruded from below the deepest levels exposed in the LHG
111 (>~7 km). Different generations of the aplite dykes either cross-cut and/or mingle with the porphyry dykes
112 (Fig. 3b) indicating that, locally, emplacement was near contemporaneous.

113

114 Despite their close temporal relationship, the porphyry and aplite dykes show very different internal textures.
115 The porphyry dykes show no direct textural evidence for fluid exsolution (e.g. miarolitic cavities⁴³), rather are
116 only seen to be cross-cut by mineralised veins. In contrast, multiple generations of aplite dykes invariably
117 contain miarolitic cavities and pegmatitic segregations that often host hypogene mineralisation (chalcocopyrite
118 ± bornite ± molybdenite), as well as early A-type veins (nomenclature after ⁴⁴) and quartz unidirectional

119 solidification textures (USTs), but are also cross-cut by mineralised veins (Fig. 3c-f & S3). The quartz USTs
120 within the aplites is likely to indicate rapid temperature or pressure fluctuations⁴⁵ and fluid exsolution via first-
121 type boiling⁴⁶, suggesting that the mineralising aplite dykes were strongly undercooled having been emplaced
122 rapidly to shallow depths. Given the aplite dykes host mineralised miarolitic cavities which are closely
123 associated with early mineralised veins (A-type⁴⁴) (Fig. 3e & 3f), they capture the nature and timing of
124 magmatic-hydrothermal fluid exsolution and mineralisation, as well as having acted as “crystal mush”
125 conduits for mineralising fluids from deep portions of the LHG³².

126

127 Field relations indicate that some parts of the Fulstone volcanics were cogenetic with the emplacement of
128 porphyry dykes associated with the LHG^{40,41}. Propylitic alteration is ubiquitous across the Fulstone Spring
129 Volcanics (e.g. epidote replacing primary plagioclase and chlorite replacing mafic minerals) (Fig. S4),
130 indicating that the hydrothermal system was active for some time after volcanism. The lack of more acidic
131 alteration (e.g. advanced argillic) indicates that these volcanics, if related, were distal to ore-forming
132 hydrothermal activity.

133

134 Absolute age constraints on porphyry system evolution

135 The determination of zircon CA-ID-TIMS U-Pb ages provides a temporal framework for the construction of
136 the Yerington batholith and eruption of overlying volcanics, over an indicated period of ~2.8 Myrs (~169.1 Ma
137 to ~166.3 Ma; Zircon ages are reported in Fig. 4 and Supplementary Data 1). The McLeod QMD (AM72 and
138 AM4QMD) and Bear QM plutons (BH10 and MA9) were emplaced over a period of >~1.6 Myrs (~169.1 Ma
139 to ~167.5 Ma). The overlapping ages of these two units indicates some degree of contemporaneous
140 emplacement, with crystallisation of their latest phases within ~100 kyrs of each other. These mineralogically
141 and texturally distinct plutons both young downwards over a palaeo-vertical distance of ~3 km, suggesting
142 under-accretion as the mode of emplacement^{e.g.47}.

143

144 For the LHG, its upper region (AM18LHG; ~5 km palaeo-depth²⁷) and a deeper portion (LH24S; ~7.5 km
145 palaeo-depth²⁷) show overlapping zircon ²⁰⁶Pb/²³⁸U dates with closely comparable weighted means of
146 167.365 ± 0.041 Ma and 167.275 ± 0.027 Ma, respectively (Fig. 4). These ages define the maximum repose
147 time between the McLeod QMD/BH and LHG of 215 ± 59 kyrs. When the 167.440 ± 0.039 Ma age of a
148 mineralised porphyry dyke (AC25) is considered, which cross-cuts the LHG cupola ~1 km higher in the
149 system than AM18LHG, then this repose time must be even shorter (140 ± 57 kyrs, or ~ 100 kyrs). The
150 crosscutting relationships imply a protracted emplacement of the exposed LHG over >~150 kyrs. These new
151 timescales also indicate that construction of the Yerington batholith was significantly longer than previously
152 estimated – meaning that long-term emplacement rates by protracted episodes of magma recharge were
153 ~two times slower than the minimum rates previously estimated³¹.

154

155 A stratigraphically lower unit of the Fulstone volcanics (BS1) yielded an age (168.318 ± 0.054 Ma; Fig. 4)
156 within the emplacement duration defined by the Bear QM and McLeod QMD, whereas the stratigraphically
157 higher unit (BS16) gave a much younger age (166.285 ± 0.059 Ma; Fig. 4), ~1.1 Myrs younger than the
158 formation of the LHG cupola. The new geochronological data supports a volcanic record that spans over ~2
159 Myrs, rather than a single post-ore volcanic event³⁴.

160
161
162
163
164
165
166
167
168
169
170
171
172
173
174
175
176
177
178
179
180

181
182
183
184
185
186
187
188
189
190
191
192
193
194
195
196
197
198
199
200

The timing of porphyry-style Cu-Mo mineralisation has been constrained from cross-cutting relationships and Re-Os molybdenite ages (Fig. 4). Ages for the mineralised porphyry dykes that cross-cut the cupolas of the LHG and the youngest ages for the McLeod QMD and Bear QM both constrain the onset of ore formation at ~167.4 Ma. The multiple generations of aplite dykes (AM63A and AM13BAP) capture the nature and timing of magmatic-hydrothermal fluid exsolution and mineralisation, and acted as conduits for the transport of mineralising fluids into the ore-forming environment³² (Fig 3 & S3). As the youngest zircon growth contained within the aplite dykes likely crystallised as part of the magmatic assemblage, the U-Pb ages of 167.282 ± 0.040 Ma and 167.045 ± 0.057 Ma (Fig. 4) offer upper limits for the mineralisation they host, showing mineralisation occurred episodically for at least ~400 kyrs.

Within the Ann Mason porphyry deposit, Re-Os molybdenite ages for a chalcopyrite-molybdenite-quartz vein (AC21) and a fine grained molybdenite vein (AC12MP) (Fig. 4 & S5; Supplementary Data 1) indicate that mineralisation occurred during multiple hydrothermal events over a period of ~600 kyrs, from 166.8 ± 0.1 to 166.2 ± 0.1 Ma. Comparison between the hydrothermal Re-Os molybdenite ages with magmatic zircon U-Pb ages requires that total uncertainties, relating to the tracer calibrations and decay constant intercalibration must be considered, which equate to ± 0.8 Myrs on Re-Os dates and $\sim \pm 0.2$ Myrs for U-Pb. Results therefore indicate porphyry-style mineralisation occurred potentially over a period in excess of 1 Myrs, roughly coincident with the eruption of the younger propylitically altered components of the Fulstone volcanics (BS16), at 166.285 ± 0.059 Ma (Fig. S4).

Geochemical change within the magmatic system

In terms of their whole-rock geochemical compositions, the McLeod QMD and Bear QM (pre-mineralised) are similar and notably different to the LHG, porphyry and aplite dykes (inter-mineralised) (Fig. 5, 6 & S6; Supplementary Data 2). The McLeod QMD and Bear QM have similar ranges in SiO₂ (~60-68 wt.%) whilst the LHG samples either overlap with these or are marginally more evolved (~67-69 wt.% SiO₂). The porphyry dykes show a range in SiO₂ (60-71 wt.%), whilst aplite dykes are the most evolved, generally having >73 wt.% SiO₂. Compared to the McLeod QMD and Bear QM, the LHG and porphyry dykes possess higher Sr/Y ratios (Sr/Y >130), steeper LREE/HREE and MREE/HREE patterns (e.g. La/Yb >30; Gd/Yb >3.7), lower ΣREEs (<100 ppm), and positive Eu anomalies (Eu/Eu* >1.05). The Dy/Yb values (~2) do not significantly change between the McLeod QMD, Bear QM and LHG.

From their whole-rock geochemistry, the pre-mineralised McLeod QMD and Bear QM are likely to be genetically related, despite their mineralogical and textural differences²⁷. A change in the bulk fractionating assemblage is indicated to yield the signatures of the inter-mineralised LHG. As previously shown²⁷, this is likely from clinopyroxene (in which Y, MREEs and HREEs are compatible, although more weakly when compared to amphibole^{48,49}) and plagioclase dominated (in which Sr and Eu are compatible⁵⁰) in the pre-mineralised units to amphibole-dominated, with the suppression of plagioclase crystallisation, in the inter-mineralised units, leading to the increased Sr/Y and Eu/Eu* values and depletion in REEs^{48,49,51} (Figs. 5 & 6).

201 Zircon geochemistry is a function of pressure, temperature and melt composition^{52,53}. During the interval of
202 zircon saturation, the composition of zircon documents these changes within the melt storage zones and
203 migration pathways. Zircon from across the Yerington magmatic system (Fig. 7 & S7-10; Supplementary
204 Data 3) can be separated into two distinct geological groups: pre-mineralisation (McLeod QMD, Bear QM
205 and older volcanic units) and inter-mineralisation (LHG, aplite dykes and younger volcanic units). Zircon Hf
206 concentrations (typically thought to reflect melt evolution⁵²) is comparable between pre- and inter-
207 mineralisation units. Zircons from the pre-mineralisation McLeod QMD and Bear QM have relatively high Ti
208 (5-20 ppm), lower Eu/Eu* (0.2-0.5) and Gd/Yb (MREE/HREE, 8-21), overlapping with the pre-mineralisation
209 Artesia volcanics and older units of the overlying Fulstone volcanics. From outer to inner portions of the
210 McLeod QMD and Bear QM, there is an increase in Gd/Yb (rising from ~10 to ~16) with decreasing zircon Ti
211 concentration. There is a step-wise change to zircon from inter-mineralised LHG and aplite dykes,
212 characterised by lower Ti (2-5 ppm), higher Eu/Eu* (~0.4 to 0.9) and Gd/Yb (~10-35). Zircons from younger
213 units of the Fulstone volcanics sit within this group.

214
215 There is no major difference in zircon composition between the LHG and aplite dykes. Zircon data of the
216 porphyry dykes show no notable trace element differences between dyke generations of the “early” and “late”
217 mineralised dykes from both the Ann Mason and Yerington porphyry copper deposits, in agreement with
218 previous zircon data from the Yerington system³⁶. Regardless of age, the porphyry dykes show no clear
219 division between the geochemical groups of pre- and inter-mineralisation plutonic rocks, which we attribute
220 to recycling of pre-mineralisation zircon grains from a magmatic system at depth. That the same zircon
221 geochemical signatures seen in the intrusive units are expressed in the volcanic terrane indicates that all
222 plutonic units were associated with volcanism.

223
224 As melt chemistry is largely linked to the composition of the source⁵⁴, major differences in zircon chemistry,
225 and by extrapolation melt chemistry, between the samples is likely to reflect differences in the source prior
226 to magma emplacement. The zircon chemistry of the McLeod QMD and Bear QM indicate a shared magmatic
227 evolution, despite their mineralogical and textural differences²⁷. The contrasting zircon geochemical signature
228 of the inter-mineralised units (LHG and aplite dykes) suggest their source underwent amphibole-dominated
229 fractionation, evidenced by the increasing MREE/HREE signature, and likely titanite fractionation, with
230 suppressed plagioclase crystallisation to give high Eu/Eu* values^{51,55}. The low Ti concentration seen in the
231 inter-mineralised zircon signature could also reflect lower temperatures within the system (as per the Ti-in-
232 zircon geothermometer⁵⁶) induced by increased melt water content and solidus suppression. Absolute
233 temperatures were not calculated from the zircons given uncertainties in the activity of TiO₂ through the
234 evolution of the magmatic system. Alternatively (or in combination), the low Ti concentration could be due to
235 decreased TiO₂ activity in the magma, due to greater incorporation of Ti into amphibole and titanite, as well
236 as possibly biotite and magnetite. Importantly, the changes shown by previous work²⁷ and whole-rock data
237 (Fig. 5 & 6) indicative of a shift from a clinopyroxene-plagioclase-dominated system to an increasingly
238 hydrous, amphibole-dominated system at the transition from a non-mineralising to mineralising magmatic
239 system is consistent with, and more pronounced, in zircon geochemistry. This changing signature can be
240 seen in both the plutonic and volcanic record.

241

242 Isotopic constraints on magma pathways

243 From a study of whole-rock $^{87}\text{Sr}/^{86}\text{Sr}_t$ ²⁷, there was a subtle transition from more radiogenic, crustal-like
244 values⁵⁷ within the pre-mineralisation intrusions to less radiogenic values within inter-mineralised intrusions,
245 indicating a decreasing amount of crustal assimilation within the magmatic system. Similarly, zircon O-
246 isotopes³⁶ also document a transition from $\delta^{18}\text{O} \sim 6 \text{‰}$, nominally above values for zircon equilibrated with
247 mantle-derived melts, indicating crustal contamination, to $\sim 4.5 \text{‰}$, more within the expected range for the
248 mantle^{58,59} (Fig. 8).

249
250 The ϵHf_t composition of the zircon used to calculate crystallisation ages, and therefore a good approximation
251 for the late-stage melt at the emplacement level, provide further insights into the evolution of the magma
252 system (Fig. 8; Supplementary Data 4). Over the period of construction of the Yerington magmatic system,
253 the main features of the data are best described by two metrics: the changes in the weighted mean ϵHf_t for
254 the sample and differences in the corresponding over-dispersion where the MSWD is in excess of that
255 expected for a single population at the stated level of uncertainty. With an ϵHf_t uncertainty of $\sim \pm 0.5 \epsilon\text{Hf}_t$ (2σ),
256 the data show that: 1) The LHG and aplite dyke samples form reproducible single populations without over-
257 dispersion indicating zircon crystallised from a melt with homogenous ϵHf , whereas the pre-mineralisation
258 samples ($>167.4 \text{ Ma}$) show over dispersion that must result from variable ϵHf between zircon and indicate
259 isotopic heterogeneity within the melt; 2) The mean value is consistent (within $\sim 0.2 \epsilon\text{Hf}_t$) for inter-
260 mineralisation samples, yet is $\sim 1 \epsilon\text{Hf}_t$ lower in the oldest Bear QM sample. The increased range and lower
261 ϵHf_t indicates greater crustal assimilation, which probably occurred during ascent into the sub-volcanic
262 environment.

263
264 Given the paucity of evidence for any significant component of zircon xenocrysts older than the Triassic
265 volcanic and sedimentary country rocks (Fig. 4 & 7; Supplementary Data 1 & 3), we infer that there was little
266 mature crustal material present to impart large variations in ϵHf_t upon assimilation. Nevertheless, there is a
267 systematic variation between earlier and later pre-mineralisation intrusions that is best explained by the pre-
268 mineralising magmas (prior to $\sim 167.4 \text{ Ma}$; McLeod QMD and Bear QM) having undergone transport, storage
269 and evolution within, and were contaminated by, the crustal column leading to the more varied and crustal
270 isotopic signatures (Sr, O and Hf). In contrast, after $\sim 167.4 \text{ Ma}$, these rocks no longer show this signature,
271 indicating no discernible assimilation of previous crust after the melts were extracted. This indicates that the
272 mineralising melts evolved within an environment where they were only exposed to a single, homogenous,
273 mantle-derived source melt prior to emplacement. This supports different evolution zones for the pre- and
274 inter-mineralisation melts. These could be either disparately within the crust, or within the same “hot-zone”⁵⁴
275 reflecting melt extraction with different proximity to the country rock, with LHG melts being entirely
276 encapsulated by the juvenile, mantle-derived rocks with negligible crustal interaction and assimilation prior
277 to emplacement

278

279 Depth of melt evolution

280 The composition of H_2O -saturated minima and eutectics (i.e. the last melt to crystallise after fractional
281 crystallisation⁶⁰) for haplogranitic melts is a function of pressure⁶¹. The pressures at which H_2O -saturated

282 melts differentiated⁵⁴ can therefore be tracked through normative mineralogy. The normative mineralogy of
283 the LHG and aplite dyke samples indicates a close relationship with the minima and for H₂O-saturated
284 haplogranitic melts⁶¹ (Fig. 9), indicating the melt from which they formed were H₂O-saturated. LHG samples
285 cluster between the ~450 MPa minima and 1000 MPa eutectic. Aplite dyke samples plot between the ~75-
286 200 MPa minima. Assuming lithostatic pressure with an average overburden density of 2.5 g/cm³, these
287 pressures roughly equate to a melt evolution depth of ~20-40 km for LHG and porphyry dykes, and ~3-8 km
288 for aplite dykes. Outliers with very little apparent orthoclase, either do not represent H₂O saturated melts,
289 have complex crystal cargoes, or were subject to overprinting Na-Ca and propylitic hydrothermal alteration
290 (as previously mapped⁴²).

291

292 These data support deep evolution of the melts which formed the LHG plutonic rocks, and likely the porphyry
293 dykes. It also indicates that following emplacement of the LHG-forming magmas from their deep (~20-40 km)
294 source to shallow levels (~3-8 km), further evolution lead to the aplite dyke forming melts which were volatile-
295 and Cu-rich (documented by fluid exsolution and mineralisation textures³²; Fig. 3 & S3).

296

297 A rapid switch to porphyry ore-forming magmas

298 The unique geological cross section of the Yerington district (Fig. 1) has recorded evidence of how magmatic
299 systems develop the potential to form Cu-porphyry deposits. In contrast to the previous emplacement models
300 for the Yerington plutonic rocks^{27,31,42}, which suggested sequential emplacement of the McLeod QMD and
301 Bear QM, the revised chronology indicates that the pre-mineralisation magmas were produced and
302 episodically emplaced over the same >1.6 Myrs period of time (Fig. 4 & 10). Whilst these units are
303 mineralogical and texturally distinct²⁷, their isotopic signatures, whole-rock and zircon geochemistry are not
304 distinct (Fig. 5-8), supporting protracted melt evolution and pathways under similar evolutionary conditions,
305 likely in a mid- to lower-crustal storage zone (~15-20 km; Fig. 10 & S11).

306

307 The most significant geochemical change within the system was an abrupt switch from signatures that
308 indicate clinopyroxene-plagioclase-dominated fractionation to an amphibole-dominated system, documented
309 within both zircon and whole-rock chemistry (Fig. 5-7 & S6-10). This change occurred between the relatively
310 evolved plutonic rocks which have comparable indicators of fractionation, such as whole-rock SiO₂ and zircon
311 Hf concentration (Fig. 6 & 7). This abrupt shift in the dominant fractionating assemblage is constrained to
312 within ~100 kyrs and is coincident with the onset of porphyry mineralisation. Following this, the mineralising
313 magmatic system was stable for potentially in excess of 1 Myrs, with the youngest magmatic activity being
314 documented within the propylitically altered volcanics, that bear the same zircon geochemical signatures as
315 the inter-mineralisation LHG samples (Fig. 4, 7 & S4).

316

317 The abrupt change in the magmatic chemistry to more hydrous and amphibole-dominated signatures can be
318 explained by a phase boundary change in the magma extracted from a single magma evolutionary zone,
319 during its longer-term progressive evolution. Within the lower crust, fractionation of anhydrous phases in the
320 relatively dry magmas, as magmatism continued over 1.6 Myrs, progressively ramped up the concentrations
321 of volatiles. The sudden change reflects the point at which the “amphibole-in” line was suddenly crossed due
322 to the volatile build up, or due to the injection of new melts into a lower crustal clinopyroxene cumulate pile
323 or “sponge”, that reacts with new melt to become progressively replaced by amphibole⁶². The dated porphyry

324 dyke that sits at the temporal onset of mineralisation (AC25; Fig. 4) and has zircon geochemistry appearing
325 to straddle the pre-and inter-mineralised signatures (Fig. 7 & S8-10) could mark this threshold being crossed.

326

327 Although we cannot rule out this transitional model to describe the evidence, there are a number of features
328 that do not support that they resulted from progression within a single magma evolution zone. For example,
329 the porphyry dykes hosted by and therefore relatively later than the LHG also contain zircon with pre-
330 mineralisation chemistry. The sharp contacts between the mineralogical distinct McLeod QMD and LHG
331 plutonics²⁷ and the temporally abrupt stepwise change in magma geochemistry following 1.6 Myrs of pre-
332 cursor magmatism is suggestive of a fundamental shift in where the melt is extracted from, rather than a
333 transition of a single melt extraction zone within the system. A scenario where a single melt extraction zone
334 suddenly changes fractionating assemblage is also challenging to reconcile given the shift in the isotopic
335 data from a heterogeneous signature, which indicates interaction with crustal components, to a
336 homogeneous more juvenile, mantle-derived signature particularly over the short timescale the data identify
337 (Fig. 8).

338

339 The abrupt, ~100 kyrs change after the >1.6 Myrs period of emplacement of the pre-mineralisation plutons
340 is better explained by a rapid switch in the magmatic plumbing system, probably within the mid- to lower-
341 crustal melt evolution zone from where the magmas feeding the upper crustal reservoir were derived (Fig.
342 10). We envisage that the earlier, pre-mineralisation stage magmas were derived from the mid- to lower-
343 crust (~15-20 km; Fig. S11). During protracted storage and evolution, these assimilated crustal material. It is
344 feasible that the contrasting nature of the McLeod QMD and Bear QM²⁷, yet in-part contemporaneous
345 emplacement periods (Fig. 4), reflect slightly different zones of storage and evolution during this period of
346 batholith growth. After the switch, magmas in the lower crustal "hot-zone"⁵⁴ (~20-40 km; Fig. 9 & 10) evolved
347 to more volatile-rich compositions which initiated the crystallisation of amphibole and/or the reaction of the
348 more hydrous melts with clinopyroxene in a mush or pre-existing cumulate pile. The more evolved melts
349 tapped from this zone had only interacted with precursor mantle-derived magmas, and possibly cumulates,
350 explaining their lack of crustal isotopic signatures (Fig. 8). In this scenario the pre-mineralisation geochemical
351 signature of the zircon cargo of the porphyry dykes would be acquired as they punched up through the pre-
352 cursor magmatic system on route to their emplacement levels.

353

354 Although there is little distinction between the LHG and porphyry dykes in terms of whole-rock geochemistry
355 (Fig. 5 & S6), from differences in their zircon trace element compositions and isotopes (Fig. 7 & 8),
356 comparable melt minima barometry (Fig. S11) along with the paucity of field evidence, it is very unlikely that
357 the porphyry dykes were derived from the upper parts of the LHG (as per previous models^{e.g.27}). From textural
358 evidence (Fig. S2), once emplaced at shallow crustal levels, the magmas underwent further magmatic
359 differentiation (at ~ 3-8 km depth, based on melt minima plots; Fig. 9) to form the more evolved and volatile-
360 rich melts that were episodically injected as undercooled aplite dykes over a period of at least ~400 kyrs.
361 Multiple generations of aplite dykes acted as crystal mush conduits for the mineralising fluids³², episodically
362 over time periods potentially in excess of ~1 Myrs post-emplacement of the LHG cupola (Figs. 3, 4 & S3), as
363 magma and volatile transport was likely decoupled. This suggests that relatively evolved, internal parts of the
364 LHG produced the magmas and associated fluids responsible for porphyry deposit formation rather than the
365 carapace of the pluton.

366
367
368
369
370
371
372
373
374
375

The proposed time-period for porphyry ore formation, which is likely to have exceeded 1 Myrs post emplacement of the LHG, is not uncommon for medium to large scale, composite porphyry systems^{e.g.24,63-65}. Given the similar zircon trace element geochemistry between mineralised porphyry dykes in the Ann Mason and Yerington porphyry deposits³⁶ (Fig. S8-10), along with their petrographic similarities²⁷, they are most likely co-genetic. It is probable that these are also co-cogenetic with porphyry dykes in the Yerington districts' two other known porphyry deposits: Bear and MacArthur. It is therefore salient for future numerical models and computational simulations of batholith construction and porphyry mineralisation to include fluids derived from across all porphyry centres, which would produce a considerably larger copper endowment.

376 Genetic implications for porphyry deposit-forming magmatic 377 systems

378
379
380
381
382
383
384
385
386
387
388
389
390
391
392
393
394

The apparent change in geochemistry (whole-rock and zircon) as the Yerington system began to produce porphyry deposits is consistent with observations across a wide range of global localities where precursor magmatism and syn-mineralisation intrusions have been examined^{e.g.19,20,22,25,66}. Typically these changes have been interpreted as being due to long-term, arc-scale, transitional “ramp-ups” towards ore-formation over millions of years^{e.g.11,16,21,23}, however this model was constrained by limited exposure in most systems²⁹. Our detailed studies of the considerably better-exposed Yerington batholith suggest that the switch to porphyry deposit-producing magmatism was at least an order of magnitude faster than previously thought. The short timescale of the geochemical changes suggested here does not necessarily contradict longer-term progressions towards hydrous, ore-forming arc magmas seen in other magmatic systems. The longer durations documented in other systems between precursor and ore-related magmatism, and their corresponding changes in geochemistry, may simply relate to the juxtaposition of upper crustal magmatic expressions over the protracted duration of the magmatic system. For example, when temporally comparing dyke to host rock in Yerington, there is a difference of up to ~1.7 Myrs for dykes that intruded up through the LHG and into shallower levels of the McLeod QMD. This means the footprint of ore-bearing systems may differ with exposure level – at shallower levels the record would look discrete and appear to develop over longer timescales, whereas at depth the system appears more concurrent.

395
396
397
398
399
400
401

We, however, recognise that a wholesale change in the deeper magmatic system occurs at a resolution which can be used to isolate geochemical signatures in the rock record. The timescale of this process appears to be beyond a multi-million year magmatic “ramp-up” driven by the macro-scale tectonic regime^{11,16,21-26}. Instead, our results indicate how the magmatic systems can much more rapidly develop their ability to form porphyry copper deposits and that this must relate to processes that are driven internally by the magmatic processes of melt generation and the extraction of evolved melts within the system itself (Fig. 10).

402
403
404
405

The recognition of a rapid ~100 kyrs switch within the magmatic plumbing system requires a new approach in the interpretation of plutonic processes in ore-forming systems. The magmas responsible for ore-formation underwent different routes of evolution and were tapped from spatially independent melt zones within the lower crust compared to the magmas which formed the pre-cursor plutons. We suggest from this that the

406 processes and evolution histories of early intruded plutons cannot necessarily be used to infer whether other
407 parts of the batholith may have produced porphyry-type deposits.

408

409 Our research offers new constraints on the depth of different melt evolution zones below the Yerington
410 porphyry district, and the abrupt nature of the change between zones of melt extraction at the onset of
411 mineralisation. This has important implications for models of batholith construction, the formation of porphyry-
412 type deposits and the development of porphyry exploration indicators. This is mainly because the short-
413 timescale over which the geochemical signatures associated with mineralisation appeared throughout the
414 magmatic system, in plutons, dykes and volcanics, significantly narrows the temporal window for ore
415 formation. This increases the potential efficacy of using these geochemical signatures to isolate areas
416 prospective for porphyry-style mineralisation. This greater confidence in the resolution of these signatures is
417 important in aiding discovery of the next generation of porphyry deposits, which are likely to be deeper and
418 often under cover and so will be more difficult to find¹⁰. Such discoveries are vital for the supply of certain
419 new technology metals which are crucial to the growth of green economies.

420

421 Conclusions

422 Using the unique and archetypal geological section of the Yerington district, the timing of batholith
423 construction, magmatic evolution and magmatic-hydrothermal mineralisation has been constrained. By doing
424 so we have identified an abrupt change in whole-rock and zircon geochemistry at the onset of porphyry
425 mineralisation. This relates to a rapid switch in the magma plumbing system to tap a deep-seated, volatile-
426 rich, zone of magma evolution in the lower crust. The rapidity of this change (~100 kyrs) shows that
427 geochemical signatures of certain plutonic and volcanic rocks can be used to interpret the specific magmatic
428 process that eventually lead to porphyry mineralisation. The results also support the contention that, in the
429 Yerington district, aplite dykes (as magmatic-hydrothermal crystal mush conduits) were the main transport
430 mechanism for porphyry-mineralising fluids from the most evolved internal portions of a voluminous upper
431 crustal pluton³². These findings provide an improved framework for new conceptual models for magmatic
432 systems and batholith construction, porphyry mineralisation, as well as relationships to volcanism. Isolating
433 short-timescale fluctuations that can be linked to abrupt changes in magmatic plumbing, from the melt
434 extraction zone within the lower crust, in addition to the longer, tectonically-driven multi-million year
435 timescales of arc-scale magmatic evolution, allows for the refinement and increased efficacy of geochemical
436 “fertility indicator” tools that extend into the volcanic environment, to aid exploration for the next generation
437 of ore deposits.

438

439 Data availability

440 All data supporting the findings of this study are available within the paper and its Supplementary files.

441

442 Acknowledgments

443 L. Carter is supported by a NERC GW4+ Doctoral Training Partnership studentship from the Natural
444 Environment Research Council [NE/L002434/1], with additional support from the Natural History Museum,
445 London and the British Geological Survey, Keyworth. This work was supported by a NERC Isotope
446 Geosciences Facilities grant [IP-1876-1118] and from the NERC Highlight Topic project “From Arc Magmas
447 to Ores (FAMOS): A Mineral Systems Approach” [NE/P017452/1]. D. Selby acknowledges the Total
448 Endowment Fund and the CUG (Wuhan) scholarship. L. Carter is thankful for additional funding from the
449 Society of Economic Geologists Foundation’s Hugh McKinstry Fund. D. First, Quaterra Resources and
450 Hudbay Resources (previously Mason Resources) are thanked for introductions, access to drill core and field
451 support. SelFrag AG are thanked for use of their EPF device. S. Pendray (Camborne School of Mines,
452 University of Exeter) and A. Wood (British Geological Survey, Keyworth) are thanked for supporting sample
453 preparation. T. Barry, L. Marvin-Dorland and A. Cox (University of Leicester) are thanked for whole-rock XRF
454 and ICP-MS analysis. J. Wilkinson (Natural History Museum, London), J. Blundy (University of Oxford) and
455 D. Smith (University of Leicester) are thanked along with other members of the FAMOS consortium for fruitful
456 proof of concept discussions.

457

458 Author Contributions

459 L.C.C and B.J.W performed field studies. L.C.C carried out petrographic and textural studies. L.C.C., S.R.T
460 and D.B.P. performed sample preparation. L.C.C. and Y.B. performed LA-ICP-MS analyses at the Natural
461 History Museum, London. S.R.T. performed zircon CA-ID-TIMS analyses and I.M. performed zircon Hf-Lu
462 isotope analyses at the British Geological Survey, Keyworth. D.S. performed molybdenite Re-Os analyses
463 at Durham University. L.C.C. wrote the first draft of the manuscript and prepared the figures. All authors
464 contributed to the final version of the manuscript.

465

466 Competing Interests

467 The authors declare no competing interests.

468

469 Methods

470 The fundamental first-order controls for this study are from field observations of cross-cutting relationships,
471 disequilibrium phenomena and textures indicative of fluid exsolution and mineralisation in outcrop across the
472 Yerington District and drillcore from the Ann Mason and Yerington porphyry copper deposits. Based on these
473 observations, select samples were chosen for whole-rock XRF and ICP-MS analysis (Supplementary Data
474 2), zircon LA-ICP-MS (Supplementary Data 3) analysis, zircon U-Pb CA-ID-TIMS and Re-Os molybdenite
475 geochronology (Supplementary Data 1) and zircon Lu-Hf isotope analysis (Supplementary Data 4).

476

477 Electric Pulse Fragmentation (EPF)

478 Initial sample preparation for subsequent whole-rock and zircon analyses was by electric pulse fragmentation
479 (EPF), also known as electrodynamic fragmentation (EDF), electrical disintegration (ED) and electric pulse
480 disaggregation (EPD)^{71,72}. EPF utilises highly energetic (150–750 J/pulse) pulsed electrical discharges with
481 a fast pulse rise time (<500 ns) to break composite materials apart along internal compositional or mechanical
482 boundaries. Samples are submerged in a dielectric process medium such as water, which is more resistive
483 than solids at these pulse rise times, resulting in the discharge being forced through the relatively conductive
484 solid and along internal phase boundaries such as mineral-mineral contacts. Each discharge event is a
485 movement of electrons from the working electrode to the ground electrode as a plasma channel^{71,73}. The
486 rapid formation of this plasma channel causes explosive expansion within the material along the discharge
487 pathway^{71,72}. In addition to direct breakage from the plasma channel, this explosion creates a shockwave that
488 propagates through the material. Varying elasticity moduli between minerals results in shear stresses being
489 focussed on mineral contact surfaces, causing intra-mineral breakage and disaggregating the rock. This
490 tensile intra-mineral breakage is less damaging to individual minerals which are liberated from the rock larger
491 and more intact than mechanical crushing.

492

493 The treatment was conducted using the 'Lab', a laboratory scale EPF device for the batch processing of
494 material, manufactured by SELFRAG AG, Switzerland. The Lab is designed to process samples of up to
495 approximately 1 L volume, or single particles with a top passing size of 40 – 45 mm in a 4 L process vessel
496 filled with de-mineralized water. It produces high voltage (90 – 200 kV) electric discharges of short duration
497 between two electrodes: the 'working' electrode is immersed in the upper part of the process vessel, while
498 the bottom of the vessel constitutes the 'counter/grounding' electrode. The operating parameters that can be
499 changed are the discharge voltage, electrode gap, pulse repetition rate and number of electric pulses applied
500 to the sample, with treatment conditions for this work listed in Table 1. Further information on the Lab system
501 can be found in ⁷⁴.

502

503 *Table 1 Treatment conditions for electric pulse fragmentation.*

Vessel (open/closed)	Sieve Aperture	Voltage	Pulse Repetition Rate	Electrode Gap	Pulses Per Cycle
Open	2 mm	180 kV	5 Hz	40 mm	100

504

505 Samples were manually crushed to 40 – 45 mm to fit into the process vessel. From optical studies the zircons
506 have an average grain diameter of ~250 microns which guided selection of an appropriate aperture sieve for

507 the SELFRAG open process vessel. Appropriate sieve aperture diameter is generally equal to 10x the target
508 particle diameter. A series of 100 pulses were applied to the sample followed by visual inspection of the
509 remaining sample; if >10 % of the sample remained above the sieve, another cycle of 100 pulses were
510 administered. When >90 % of sample material had passed through the sieve, treatment was stopped, and
511 the sample recovered from the process vessel collection cup before drying at 70°C.

512

513 Whole-Rock XRF and ICP-MS analysis, and CIPW Normative Mineralogy

514 Fully quantitative X-ray fluorescence (XRF) for whole-rock geochemistry was performed at the University of
515 Leicester's Department of Geology on a PANalytical Axios Advanced XRF spectrometer. Major elements
516 were determined on fused glass beads (prepared from ignited powders; sample to flux ratio 1:5, 80% Li
517 metaborate: 20% Li tetraborate flux) and trace elements were analysed on pressed powder briquettes (32
518 mm diameter; 7.5 g sample mixed with 15-20 drops 7% PVA solution as binding agent, pressed at 10 tons
519 per sq. inch). Major element results were quoted as component oxide weight percent, re-calculated to include
520 loss on ignition (LOI). Information on the standards analysed and the accuracy and precision of the XRF
521 analysis is available in Supplementary Data 2.

522

523 Inductively coupled plasma mass spectrometry (ICP-MS) for whole-rock trace element geochemistry was
524 also performed at the University of Leicester's Department of Geology on a ThermoScientific ICAP-Qc
525 quadrupole ICP mass spectrometer. Analysis for rare earth elements (REEs), Hf, Sr and Y was performed
526 on solution from the same fused glass beads used for XRF analysis. Information on the standards analysed
527 and the accuracy and precision of the ICP-MS analysis is available in Supplementary Data 2.

528

529 Whole-rock XRF geochemistry was used to calculate CIPW normative mineralogy (method of ⁷⁰, after ⁷⁵).
530 Normative mineralogy data was then plotted on the H₂O-saturated melt minima ternary plot⁶¹ to estimate the
531 pressures of melt differentiation⁵⁴ of H₂O-saturated melts. Assuming lithostatic conditions, pressures from
532 this plot were used to equate approximate depths of melt differentiation using $P = \rho gh$ and assuming an
533 average overburden density of 2.5 g/cm³.

534

535 Zircon Separation

536 Zircons were separated from disaggregated samples at the British Geological Survey, Keyworth, using the
537 sequentially described circuit: Sieve to <500 µm using a Fritsch automatic sieve; Pass the <500 µm fraction
538 over a Gemini water table, twice; Separate non-magnetic minerals using a Frantz isodynamic separator -
539 subsequent paramagnetic charges of 0.1 A, 0.3 A, 0.7 A, 1.1 A and 1.7 A were used to reduce the bulk
540 material in stages; Perform gravity separation utilising methylene iodide (ca. 3.32 SG) as a density medium.
541 The final zircon (amongst other phases) separate was thermally annealed at 900°C for 12 hours. Annealed
542 zircon grains were then picked by hand and prepared as polished blocks. Cathodoluminescence (CL) images
543 of these were generated by SEM-CL, using an FEI Quanta 650F FEG-SEM equipped with a Gatan
544 monochrome CL detector at the University of Exeter's Environment and Sustainability institute operating at
545 an accelerating voltage of 20 kV, as well as using a CITL Mk5 electron source, operating at approximately
546 250 µA and 10 kV. For the latter, images were captured using a Nikon DS-Ri2 camera, attached to a
547 petrographic microscope, and operated using NiS-elements software. Images were captured in a darkened
548 room, with an exposure time of 2 seconds.

549

550 Zircon LA-ICP-MS

551 Zircon cores and rims were analysed for their trace element geochemistry in the LODE Laboratory at the
552 Natural History Museum, London, using an ESI (New Wave Research) NWR193 excimer laser coupled to
553 an Agilent 7700x quadrupole ICP-MS. Individual zircon grains were located using images obtained by cold-
554 cathode CL and SEM-CL at Camborne School of Mines. A spot size of 30 μm was used and ablation was
555 performed at a repetition rate of 5 Hz and fluence of 3.5 J/cm². For each spot, approximately 20 seconds of
556 background signal followed by 40 seconds of signal acquisition during ablation. Analytical conditions,
557 including isotopes measured and dwell times are summarised in Supplementary Data 3.

558

559 Zircon U-Pb CA-ID-TIMS geochronology

560 Chemical abrasion isotope dilution thermal ionization mass spectrometry (CA-ID-TIMS) U-Pb zircon
561 geochronology was undertaken at the Geochronology and Tracers Facility, British Geological Survey,
562 Keyworth. After thermal annealing at 900°C zircon were chemically abraded at 190 °C for 12 hours following
563 ⁷⁶. The methodology for all other analytical procedures, instrumental conditions, corrections and data
564 reduction follows that outlined in detail in ⁷⁷ using the ET(2)535 tracers^{78,79}. Isotope ratio measurements were
565 made using a Thermo Triton thermal ionization mass-spectrometer (TIMS), with the U decay constants of ⁸⁰,
566 the ²³⁸U/²³⁵U ratio of ⁸¹, and the decay constants for ²³⁰Th of ⁸². The ²⁰⁶Pb/²³⁸U dates were corrected for initial
567 ²³⁰Th disequilibrium⁸³ upon zircon crystallisation using the zircon/melt partition coefficient $f_{\text{Th/U}}$ of 0.246⁸⁴.
568 Results are reported in Supplementary Data 1.

569

570 The estimate of crystallisation ages are selected from the ²⁰⁶Pb/²³⁸U (Th corrected) weighted mean of the
571 youngest population of data where the date had a statistically acceptable MSWD (Mean square of weighted
572 deviates) for the given population size and attributed 2 σ uncertainties, indicating that any dispersion between
573 the selected analyses can be attributable to the measurement of a single population. All samples, with the
574 exception of the volcanic sample BS1, display over-dispersion between the dates of individual zircons or
575 zircon fragment dates in excess of that expected due to analytical scatter. Dates that are older than the
576 statistically valid weighted mean single population are attributed to antecrystic zircon growth, either being
577 sourced from deeper within the magmatic system than the emplacement level or due to protracted
578 crystallisation of zircon upon emplacement. To further evaluate the sensitivity of the age interpretation to the
579 selection of dates we evaluated two further scenarios of date calculation: 1) Selecting the youngest date as
580 being representative of youngest zircon growth; 2) selecting the weighted mean date of the youngest three
581 dates that give a statistically acceptable MSWD. These evaluations of date selections are provided in
582 Supplementary Data 1, and illustrate that regardless of the approach adopted the timescales we discuss are
583 robust.

584

585 When comparing dates either internally or to other data sets that are undertaken with the Earthtime mixed
586 U-Pb tracers^{78,79} only the analytical uncertainties need to be considered. To evaluate U-Pb dates against
587 other isotopic systems, systematic uncertainties must also be acknowledged within the interpretation. The
588 total uncertainty including systematic components from tracer calibration and decay constants are provided
589 with age interpretations in Supplementary Data 1. For comparison with the Re-Os dates where they include

590 the Re-Os decay constant uncertainty we recommend that only the tracer calibration uncertainty is
591 considered for the U-Pb data as $\lambda^{187}\text{Re}$ is derived from inter-calibration with U-Pb data^{85,86}.

592

593 Zircon Lu-Hf Isotopes

594 The Lu-Hf fractions were obtained from elements eluted under 3M HCl within the ion exchange U and Pb
595 purification scheme during CA-ID-TIMS U-Pb analysis^{e.g.87}. Results of the Lu-Hf isotope analysis
596 (Supplementary Data 4) therefore correspond to the same volume of material as the associated zircon U-Pb
597 date. By selecting zircon from the young weighted mean population this provides temporal constraints that
598 the volume best captures the nature of the melt upon emplacement. The Lu and Hf elution was dried at 70°C
599 to a chloride before being dissolved in 1 ml of 2% HNO₃ + 0.1M HF, prior to analysis on a Thermo-Electron
600 Neptune Plus mass spectrometer, using a Cetac Aridus II desolvating nebuliser. 0.006 l/min of nitrogen were
601 introduced via the nebulizer in addition to Ar in order to minimise oxide formation. The instrument was
602 operated in static multicollection mode, with cups set to monitor ¹⁷²Yb, ¹⁷³Yb, ¹⁷⁵Lu, ¹⁷⁶Lu+Hf+Yb, ¹⁷⁷Hf, ¹⁷⁸Hf,
603 ¹⁷⁹Hf and ¹⁸⁰Hf. 1% dilutions of each sample were tested prior to analysis, and samples diluted to c. 20ppb.
604 Standard sample cones and X-skimmer cones were used, giving a typical signal of c. 800-1000 V/ppm Hf.
605 Correction for ¹⁷⁶Yb on the ¹⁷⁶Hf peak was made using reverse-mass-bias correction of the ¹⁷⁶Yb/¹⁷³Yb ratio
606 empirically derived using Hf mass-bias corrected Yb-doped JMC475 solutions⁸⁸. ¹⁷⁶Lu interference on the
607 ¹⁷⁶Hf peak was corrected by using the measured ¹⁷⁵Lu and assuming ¹⁷⁶Lu/¹⁷⁵Lu = 0.02653. Data are reported
608 relative to ¹⁷⁹Hf/¹⁷⁷Hf = 0.7325. The Hf standard solution JMC475 was analysed during each analytical
609 session and sample ¹⁷⁶Hf/¹⁷⁷Hf ratios are reported relative to a value of 0.282160 for this standard⁸⁸. Eleven
610 analyses of JMC475 gave a mean ¹⁷⁶Hf/¹⁷⁷Hf value of 0.282146 ± 0.000007 (1σ). Typical external precision
611 was in the range between 13-22 ppm. Data were reduced with an in-house calculation and time corrected
612 values include uncertainty propagated from the weighted mean date of the sample.

613

614 Rhenium-Osmium molybdenite geochronology

615 Molybdenite Re-Os ages were determined for a quartz-chalcopyrite-molybdenite quartz vein (sample AC12)
616 and molybdenite paint vein (sample AC21MP) sampled from drill core from the Ann Mason porphyry deposit.
617 Sample details in Supplementary Data 1 and Fig. S5.

618

619 The Re-Os molybdenite analysis were carried out in the Source Rock and Sulfide Geochemistry and
620 Geochronology, and Arthur Holmes Laboratories at University of Durham (United Kingdom) to establish the
621 Re-Os age of molybdenite mineralisation. A total of five analyses were conducted. One from sample AC12
622 and four from sample AC21MP (For which sample AC21MP was approximately split into four equal
623 subsamples; Fig. S5). Pure molybdenite separates were obtained from the silicate matrix was achieved using
624 the HF purification method⁸⁹, and then further purified (removal of any pyrite and/or chalcopyrite and
625 undissolved silicate phases) by hand under a binocular microscope.

626

627 An aliquant of the molybdenite separate (~20 mg) together with a known amount of tracer solution (¹⁸⁵Re +
628 Os bearing a normal isotope composition) were placed into a carius tube and digested with 3mL HCl and
629 6mL HNO₃ at 220°C for 23 hrs. Osmium was isolated and purified using solvent extraction (CHCl₃) and micro-
630 distillation methods, with the resulting Re-bearing fraction purified using NaOH-Acetone solvent extraction

631 and anion chromatography^{90,91}. Although negligible in comparison to the Re and Os abundance in the
632 molybdenite, the final Re-Os data are blank corrected. A full analytical protocol blank run parallel with the
633 molybdenite analysis yields 3.9 pg Re and 0.5 pg Os, the latter possessing a ¹⁸⁷Os/¹⁸⁸Os composition of 0.21
634 ± 0.2. Data treatment follows that outlined in ⁹¹. All Re-Os data are given with 2σ absolute uncertainties
635 (Supplementary Data 1). Molybdenite Re-Os ages are calculated using a ¹⁸⁷Re decay constant of 1.666×10⁻¹¹
636 y⁻¹ with an uncertainty of 0.31%^{85,86}. The Henderson molybdenite reference material (RM8599) analyzed
637 during the course of this study yields a Re-Os age of 27.62 ± 0.11 (2σ; n = 1), which is in good agreement
638 with the recommended value of 27.66 ± 0.10 Ma⁹²⁻⁹³, and that reported by ⁹¹ (27.695 ± 0.038 Ma, n = 9) and
639 previous analysis at Durham (e.g., 27.65 ± 0.12 Ma⁸⁹).
640

References

- 642 1. Jowitt, S. M., Mudd, G. M. & Thompson, J. F. H. Future availability of non-renewable metal resources and the influence of
643 environmental, social, and governance conflicts on metal production. *Commun Earth Environ* **1**, 13 (2020).
644 <https://doi.org/10.1038/s43247-020-0011-0>
645
646 2. Herrington, R. Mining our green future. *Nat. Rev. Mater.* (2021). <https://doi.org/10.1038/s41578-021-00325-9>
647
648 3. Elshkaki, A., Graedel T. E., Ciacci, L. & Reck, B. K. Copper demand, supply, and associated energy use to 2050. *Global*
649 *Environmental Change* **39**, 305-315 (2016). <https://doi.org/10.1016/j.gloenvcha.2016.06.006>
650
651 4. Watari, T., Nansai, K. & Nakajima, K. Major metals demand, supply, and environmental impacts to 2100: A critical review.
652 *Resources, Conservation and Recycling* **164**, 105107 (2021). <https://doi.org/10.1016/j.resconrec.2020.105107>
653
654 5. Sillitoe, R. H. Porphyry Copper Systems. *Econ. Geol.* **105**, 3-41 (2010). <https://doi.org/10.2113/gsecongeo.105.1.3>
655
656 6. Richards, J. P. Cumulative factors in the generation of giant calc-alkaline porphyry Cu deposits. In: Porter, T.M. (ed.), Super
657 porphyry copper and gold deposits: A global perspective, v. 1: Adelaide, PGC Publishing, 7-25 (2005).
658
659 7. Wilkinson, J. J. Triggers for the formation of porphyry deposits in magmatic arcs. *Nature Geoscience* **6**, 917-925 (2013).
660 <https://doi.org/10.1038/ngeo1940>
661
662 8. Richards, J. P. Tectonic, magmatic, and metallogenic evolution of the Tethyan orogen: From subduction to collision. *Ore*
663 *Geol. Rev.* **70**, 323-345 (2015). <https://doi.org/10.1016/j.oregeorev.2014.11.009>
664
665 9. Cashman, K. V., Stephen, R. J. & Blundy, J. D. Vertically extensive and unstable magma systems: A unified view of igneous
666 processes. *Science* **355**, 6331 (2017). <https://doi.org/10.1126/science.aag3055>
667
668 10. Cooke, D. R., Agnew, P., Hollings, P. *et al.* Porphyry indicator minerals (PIMS) and porphyry vectoring and fertility tools
669 (PVFTS) – Indicators of mineralisation styles and recorders of hypogene geochemical dispersion halos. In: Tschirhart, V.
670 & Thomas, M. D. (eds.) Proceedings of Exploration 17: Sixth Decennial International Conference on Mineral Exploration,
671 457-470 (2017).
672
673 11. Rohrlach, B. & Loucks, R. Multi-million-year cyclic ramp-up of volatiles in a lower crustal magma reservoir trapped below
674 the Tampakan copper-gold deposit by Mio-Pliocene crustal compression in the southern Philippines. Adelaide, PGC Publ.
675 2:369–407 (2005).
676
677 12. Richards, J. P. High Sr/Y arc magmas and porphyry Cu±Mo±Au deposits: Just add water. *Econ. Geol.* **106(7)**, 2075-1081
678 (2011). <https://doi.org/10.2113/econgeo.106.7.1075>
679
680 13. Chiaradia, M., Ulianov, A., Kouzmanov, K. *et al.* Why large porphyry Cu deposits like high Sr/Y magmas? *Sci. Rep.* **2**, 685
681 (2012). <https://doi.org/10.1038/srep00685>
682
683 14. Chiaradia, M. Crustal thickness control on Sr/Y signatures of recent arc magmas: an Earth scale perspective. *Sci.*
684 *Rep.* **5**, 8115 (2015). <https://doi.org/10.1038/srep08115>
685
686 15. Richards, J. P. High Sr/Y Magmas Reflect Arc Maturity, High Magmatic Water Content, and Porphyry Cu ± Mo ± Au
687 Potential: Examples from the Tethyan Arcs of Central and Eastern Iran and Western Pakistan. *Econ. Geol.* **107(2)**, 295-
688 332 (2012). <https://doi.org/10.2113/econgeo.107.2.295>
689
690 16. Loucks, R. R. Distinctive composition of copper-ore-forming arc magmas. *Aust. J. Earth Sci.* **61**, 5–16 (2014).
691 <https://doi.org/10.1080/08120099.2013.865676>
692
693 17. Lu, Y., Loucks, R. R., Fiorentini, M. *et al.* Zircon Compositions as a Pathfinder for Porphyry Cu ± Mo ± Au Deposits. *Society*
694 *of Economic Geologists. Special Publications Series* **19**, 329-347 (2016). <https://doi.org/10.5382/SP.19.13>
695
696 18. Williamson, B., Herrington, R. & Morris, A. Porphyry copper enrichment linked to excess aluminium in plagioclase. *Nature*
697 *Geosci.* **9**, 237–241 (2016). <https://doi.org/10.1038/ngeo2651>
698
699 19. Nathwani, C. L., Loader, M. A., Wilkinson, J. J. *et al.* Multi-stage arc magma evolution recorded by apatite in volcanic rocks.
700 *Geology* **48(4)**, 323-327 (2020). <https://doi.org/10.1130/G46998.1>
701
702 20. Lee, R. G., Byrne, K., D'Angela, M. *et al.* Using zircon trace element composition to assess porphyry copper potential of
703 the Guichon Creek batholith and Highland Valley Copper deposit, south-central British Columbia. *Miner. Deposita* **56**, 215-
704 238 (2021). <https://doi.org/10.1007/s00126-020-00961-1>
705
706 21. Ballard, J. R., Palin, J. M. & Campbell, I. H. Relative oxidation states of magmas inferred from Ce(IV)/Ce(III) in zircon:
707 application to porphyry copper deposits of northern Chile. *Contrib. Mineral. Petrol.* **144**, 347-364 (2002).
708 <https://doi.org/10.1007/s00410-002-0402-5>
709
710 22. Chiaradia, M., Meino, D. & Spikings, R. Rapid transition to long-lived deep crustal magmatic maturation and the formation
711 of giant porphyry-related mineralization (Yanacocha, Peru). *Earth. Planet. Sci. Lett.* **288**, 505-515 (2009)
712

- 713 23. Rezeau, H., Moritz, R., Wotzlaw, J. *et al.* Temporal and genetic link between incremental pluton assembly and pulsed
714 porphyry Cu-Mo formation in accretionary orogens. *Geology* **44**(8), 627–630 (2016). <https://doi.org/10.1130/G38088.1>
715
- 716 24. Chiaradia, M. & Caricchi, L. Stochastic modelling of deep magmatic controls on porphyry copper deposit endowment. *Sci.*
717 *Rep.* **7**, 44523 (2017). <https://doi.org/10.1038/srep44523>
718
- 719 25. Nathwani, C. L., Simmons A. T., Large, S. J. E. *et al.* From long-lived batholith construction to giant porphyry copper deposit
720 formation: petrological and zircon chemical evolution of the Quellaveco District, Southern Peru. *Contrib. Mineral. Petrol.*
721 **176**, 12 (2021). <https://doi.org/10.1007/s00410-020-01766-1>
722
- 723 26. Richards, J. P. Tectono-Magmatic Precursors for Porphyry Cu-(Mo-Au) Deposit Formation. *Econ. Geol.* **98**, 1515-1533
724 (2003). <https://doi.org/10.2113/gsecongeo.98.8.1515>
725
- 726 27. Dilles, J. H. Petrology of the Yerington Batholith, Nevada: Evidence for evolution of porphyry copper ore fluids. *Econ. Geol.*
727 **82**, 1750-1789 (1987).
728
- 729 28. Seedorff, E., Dilles, J. H., Proffett, J. M. *et al.* Porphyry deposits: Characteristics and origin of hypogene features. *Econ.*
730 *Geol.* **100**, 251-298 (2005).
731
- 732 29. Seedorff, E., Barton, M. D., Stavast, W. J. A & Maher, D. J. Root Zones of Porphyry Systems: Extending the Porphyry
733 Model to Depth. *Econ. Geol.* **103**, 939-956 (2008).
734
- 735 30. Weis, P., Driesner, T. & Heinrich, C. A. Porphyry-copper ore shells form at stable pressure-temperature fronts within
736 dynamic fluid plumes. *Science* **338**, 1613-1616 (2012). <https://doi.org/10.1126/science.1225009>
737
- 738 31. Schöpa, A., Annen, C., Dilles, J. H., Sparks, R. S. J. & Blundy, J. D. Magma emplacement rates and porphyry copper
739 deposits: Thermal modeling of the Yerington Batholith, Nevada. *Econ. Geol.* **112**, 1653-1672 (2017).
740 <https://doi.org/10.5382/econgeo.2017.4525>
741
- 742 32. Carter, L. C., Williamson, B. J., Tapster, S. R. *et al.* Crystal mush dykes as conduits for mineralising fluids in the Yerington
743 porphyry copper district, Nevada. *Commun. Earth Environ.* **2**, 59 (2021). <https://doi.org/10.1038/s43247-021-00128-4>
744
- 745 33. Proffett, J. M. Cenozoic geology of the Yerington district, Nevada, and implications for the nature and origin of Basin and
746 Range faulting. *GSA Bull.* **88**(2), 247-266 (1977).
747
- 748 34. Dilles, J. H. & Wright, J. E. The chronology of early Mesozoic arc magmatism in the Yerington district of western Nevada
749 and its regional implications. *GSA Bull.* **100**(5), 644-652 (1988).
750
- 751 35. Dilles, J. H. & Proffett, J. M. Metallogensis of the Yerington batholith, Nevada. *In: Pierce, F. W., & Bolm, J. G. (Eds.),*
752 *Porphyry copper deposits of the American cordillera: Arizona Geological Society Digest*, **20**, 306–315 (1995).
753
- 754 36. Banik, T. J., Coble, M. A. & Miller, C. F. Porphyry Cu formation in the middle Jurassic Yerington batholith, Nevada, USA:
755 Constraints from laser Raman, trace element, U-Pb age, and oxygen isotope analyses of zircon. *Geosphere* **13**(4), 1113-
756 1132 (2017). <https://doi.org/10.1130/GES01351.1>
757
- 758 37. Bryan, R. C. NI 43-101 Technical Report Mineral Resource Update Yerington Copper Project Lyon County, Nevada.
759 *TetraTech* (2014). Available: <https://quaterra.com/projects/quaterras-yerington-copper-projects/yerington-deposit/>.
760
- 761 38. Henderson, M. R., Byan, R. C., Welhener, H. E., Jolk, R. W. & Willow, M. A. MacArthur Copper Project; Amended NI 43-
762 101 Technical Report Preliminary Economic Assessment. *M3 Engineering*. [https://quaterra.com/projects/quaterras-](https://quaterra.com/projects/quaterras-yerington-copper-projects/macarthur-copper-deposit/)
763 [yerington-copper-projects/macarthur-copper-deposit/](https://quaterra.com/projects/quaterras-yerington-copper-projects/macarthur-copper-deposit/) (2014).
764
- 765 39. Hudbay Minerals Inc. Mason Preliminary Economic Assessment Summary. [https://hudbayminerals.com/investors/press-](https://hudbayminerals.com/investors/press-releases/press-release-details/2021/Hudbay-Announces-Positive-Preliminary-Economic-Assessment-for-its-Mason-Copper-project/default.aspx)
766 [releases/press-release-details/2021/Hudbay-Announces-Positive-Preliminary-Economic-Assessment-for-its-Mason-](https://hudbayminerals.com/investors/press-releases/press-release-details/2021/Hudbay-Announces-Positive-Preliminary-Economic-Assessment-for-its-Mason-Copper-project/default.aspx)
767 [Copper-project/default.aspx](https://hudbayminerals.com/investors/press-releases/press-release-details/2021/Hudbay-Announces-Positive-Preliminary-Economic-Assessment-for-its-Mason-Copper-project/default.aspx) (2021).
768
- 769 40. Proffett, J. M. Report on the geology and genesis of the Yerington porphyry copper district, Nevada, a four dimensional
770 study. *Final report for: USGS mineral resource external research program grant 06HQGR0171* (2007).
771
- 772 41. Proffett, J. M. High Cu grades in porphyry Cu deposits and their relationship to emplacement depth of magmatic sources.
773 *Geology* **37**(8), 675-378 (2009). <https://doi.org/10.1130/G30072A.1>
774
- 775 42. Dilles, J. H., Einaudi, M. T., Proffett, J. & Barton, M. D. Overview of the Yerington Porphyry Copper District: Magmatic to
776 Nonmagmatic Sources of Hydrothermal Fluids, Their Flow Paths, Alteration Effects on Rocks, and Cu-Mo-Fe-Au Ores.
777 *Society of Economic Geologists Guidebook Series* **32**, 55-66 (2000). <https://doi.org/10.5382/GB.32>
778
- 779 43. Candela, P. A. A review of shallow, ore-related granites: Textures, volatiles, and ore metals. *J. Petrol.* **38**(12), 1619-1633
780 (1997).
781
- 782 44. Gustafson, L. B. & Hunt, J. P. The porphyry copper deposit at El Salvador, Chile. *Econ. Geol.* **70**, 857-912 (1975).
783
- 784 45. Kirwin, D. J. Unidirectional solidification textures associated with intrusion-related Mongolian mineral deposits. *In:*
785 *Seltmann, R., Gerel, O., & Kirwin, D.J., (eds.), Geodynamics and metallogeny of Mongolia with special emphasis on copper*
786 *and gold deposits: Society of Economic Geologists-International Association for the Genesis of Ore Deposits Field Trip,*
787 *2005: IAGOD Guidebook Series 11: London, Centre for Russian and Central EurAsian Mineral Studies, Natural History*

- 788 Museum, 63–84 (2005).
789
790
791 46. Candela, P. A. Felsic magmas, volatiles, and metallogenesis. *In: Whitney, J. A. & Naldrett, A. J. (Eds.), Ore Deposition*
792 *Associated with Magmas. Reviews in Economic Geology*, 223-233 (1989).
793
794 47. Menand, T. Physical controls and depth of emplacement of igneous bodies: A review. *Tectonophysics* **500(1-4)**, 11-19
795 (2011). <https://doi.org/10.1016/j.tecto.2009.10.016>
796
797 48. Luhr, J. F., Carmichael, I. S. E. & Varekamp, J. C. The 1982 eruptions of El Chichón Volcano, Chiapas, Mexico: Mineralogy
798 and petrology of the anhydrite-bearing pumices. *J. Volcanol. Geotherm.* **23(1-2)**, 69-108 (1984).
799 [https://doi.org/10.1016/0377-0273\(84\)90057-X](https://doi.org/10.1016/0377-0273(84)90057-X)
800
801 49. Nandedkar, R. H., Hürlimann, N., Ulmer, P. & Müntener, O. Amphibole–melt trace element partitioning of fractionating
802 calc-alkaline magmas in the lower crust: an experimental study. *Contrib. Mineral. Petrol.* **171**, 71 (2016).
803 <https://doi.org/10.1007/s00410-016-1278-0>
804
805 50. Aigner-Torres, M., Blundy, J., Ulmer, P. & Pettke, T. Laser Ablation ICPMS study of trace element partitioning between
806 plagioclase and basaltic melts: An experimental approach. *Contrib. Mineral. Petrol.* **153**, 647–667 (2007).
807 <https://doi.org/10.1007/s00410-006-0168-2>
808
809 51. Sisson, T. W. Hornblende–melt trace-element partitioning measured by ion microprobe. *Chemical Geology* **117(1-4)**, 331-
810 344 (1994).
811
812 52. Claiborne, L. L., Miller, C. F., Walker, B. A. *et al.* (2006) Tracking magmatic processes through Zr/Hf ratios in rocks and
813 Hf and Ti zoning in zircons: An example from the Spirit Mountain batholith, Nevada. *Mineral. Mag.* 70:517–543 (2006).
814
815 53. Burnham, A. Key concepts in interpreting the concentrations of the rare earth elements in zircon. *Chem. Geol.* **551**, 119765
816 (2020). <https://doi.org/10.1016/j.chemgeo.2020.119765>
817
818 54. Annen, C., Blundy, J. D. & Sparks R. S. J. The Genesis of Intermediate and Silicic Magmas in Deep Crustal Hot Zones.
819 *Jour. Petrol.* **47(3)**, 505-539 (2006). <https://doi.org/10.1093/petrology/eqi084>
820
821 55. Loader, M. A., Wilkinson, J.J. & Armstrong, R. N. The effect of titanite crystallisation on Eu and Ce anomalies in zircon
822 and its implications for the assessment of porphyry Cu deposit fertility. *Earth Planet. Sci. Lett.* **472**, 107-119 (2017).
823 <https://doi.org/10.1016/j.epsl.2017.05.010>
824
825 56. Watson, E. B. & Harrison, T. M. Zircon thermometer reveals minimum melting conditions on earliest earth. *Science* **308**,
826 841-844 (2005). <https://doi.org/10.1126/science.1110873>
827
828 57. Taylor, H. P. The effects of assimilation of country rocks by magmas on ¹⁸O/¹⁶O and ⁸⁷Sr/⁸⁶Sr systematics of igneous
829 rocks. *Earth. Planet. Sci. Lett.* **47**, 243-254 (1980).
830
831 58. Valley, J. W. Oxygen isotopes in zircon. *Rev. Mineral. Geochem.* **53(1)**, 343-385 (2003). <https://doi.org/10.2113/0530343>
832
833 59. Bindeman, I. Oxygen isotopes in mantle and crustal magmas as revealed by single crystal analysis. *Rev. Mineral.*
834 *Geochem.* **69**, 445-478 (2008). <https://doi.org/10.2138/rmg.2008.69.12>
835
836 60. Tuttle, O. F. & Bowen, N. L. Origin of granite in the light of experimental studies in the system NaAlSi₃O₈-KAlSi₃O₈-SiO₂-
837 H₂O. *Geol. Soc. Am. Mem.* **74**, 153 (1958).
838
839 61. Blundy, J. & Cashman, K. Ascent-driven crystallisation of dacite magmas at Mount St Helens, 1980-1986. *Contrib. Mineral.*
840 *Petrol.* **140**, 631-650 (2001). <https://doi.org/10.1007/s004100000219>
841
842 62. Smith, D. Clinopyroxene precursors to amphibole sponge in arc crust. *Nat. Commun.* **5**, 4329 (2014).
843 <https://doi.org/10.1038/ncomms5329>
844
845 63. Romero, B., Kojima, S., Wong, C. *et al.* Molybdenite mineralization and Re-Os geochronology of the Escondida and
846 Escondida Norte porphyry deposits, Northern Chile. *Resour. Geol.* **61(1)**, 91-100 (2010). <https://doi.org/10.1111/j.1751-3928.2010.00150.x>
847
848 64. Stein H. J. Dating and Tracing the History of Ore Formation. *In: Holland H. D. and Turekian K. K. (eds.) Treatise on*
849 *Geochemistry, Second Edition*, **13**, 87-118. Oxford: Elsevier (2014).
850
851 65. Chang, J., Li, J.-W., Selby, D., Liu, J.-C. & Deng, X.-D. Geological and chronological constraints on the long-lived Eocene
852 Yulong porphyry Cu-Mo deposit, eastern Tibet, China: implications for lifespan of magmatic-hydrothermal processes
853 forming giant and supergiant porphyry Cu deposits. *Econ. Geol.* **112(7)**, 1719-1746 (2017).
854 <https://doi.org/10.5382/econgeo.2017.4527>
855
856 66. Dilles, J. H., Kent, A. J. R., Wooden, J. L. *et al.* (2015) Zircon compositional evidence for sulfur-degassing from ore-forming
857 arc magmas. *Econ. Geol.* **110**, 241–251 (2015). <https://doi.org/10.2113/econgeo.110.1.241>
858
859 67. Hudson, D. M. & Oriol, W. M. Geologic map of the Buckskin Range, Nevada. Nevada Bureau of Mines and Geology, map
860 64 (1979).
861
862 68. Proffett, J. M. & Dilles, J. H. Geological map of the Yerington district, Nevada: Nevada Bureau of Mines and Geology, map

- 863 77 (1984).
864
865 69. McDonough, W. F. & Sun, S. S. The composition of the Earth. *Chem. Geol.* **120**, 223-253 (1995).
866
867 70. Lowenstern, J. B. C.I.P.W. norm. Calculator. USGS (2000).
868 https://volcanoes.usgs.gov/observatories/yvo/jlowenstern/other/software_jbl.html
869
870 71. Andres, U., Jirestig, J. & Timoshkin, I. Liberation of minerals by high-voltage electrical pulses, *Powder Technology* **104**,
871 37–49 (1999). [https://doi.org/10.1016/S0032-5910\(99\)00024-8](https://doi.org/10.1016/S0032-5910(99)00024-8)
872
873 72. Bluhm, H., Frey, W., Giese, H. *et al.* Application of pulses HV discharges to material fragmentation and recycling, IEEE
874 *Trans. Dielectr. Electr. Insul.* **7**, 625–636, (2000).
875
876 73. van der Wielen, K. P. Application of high voltage breakage to a range of rock types of varying physical properties. Ph.D.
877 thesis, Camborne School of Mines, University of Exeter, UK (2013).
878
879 74. Bru, K., Beaulieu, M., Sousa, R., *et al.* 2020. Comparative laboratory study of conventional and Electric Pulse
880 Fragmentation (EPF) technologies on the performances of the comminution and concentration steps for the beneficiation
881 of a scheelite skarn ore. *Minerals Engineering* **150**, 106302 (2020). <https://doi.org/10.1016/j.mineng.2020.106302>
882
883 75. Kelsey, C. H. Calculation of the C.I.P.W. norm. *Mineral. Mag.* **34**, 276-282 (1965).
884
885 76. Mattinson, J. M. Zircon U-Pb chemical abrasion (“CA-TIMS”) method: Combining annealing and multi-step partial
886 dissolution analysis for improved precision and accuracy of zircon ages. *Chem. Geol.* **220(1-2)**, 47-66 (2005).
887 <https://doi.org/10.1016/j.chemgeo.2005.03.011>
888
889 77. Tapster, S., Condon, D.J., Naden, J. *et al.* Rapid thermal rejuvenation of high-crystallinity magma linked to porphyry copper
890 deposit formation; evidence from the Koloula Porphyry Prospect, Solomon Islands. *Earth. Planet. Sci. Lett.* **442**, 206-217
891 (2016). <https://doi.org/10.1016/j.epsl.2016.02.046>
892
893 78. Condon, D. J., Schoene, B., McLean, N. M., *et al.* Metrology and Traceability of U-Pb Isotope Dilution Geochronology
894 (EARTHTIME Tracer Calibration Part I). *Geochim. Cosmochim. Acta.* **164**, 464-480 (2015).
895 <https://doi.org/10.1016/j.gca.2015.05.026>
896
897 79. McLean, N. M., Condon, D. J. Schoene, B. & Bowring, S. A. Evaluating uncertainties in the calibration of isotopic reference
898 materials and multi-element isotopic tracers (EARTHTIME Tracer Calibration Part II). *Geochim. Cosmochim. Acta.* **164**,
899 481-501 (2015). <https://doi.org/10.1016/j.gca.2015.02.040>
900
901 80. Jaffey, A. H., Flynn, K. F., Glendenin, L. E. *et al.* Precision Measurement of Half-Lives and Specific Activities of U-235 and
902 U-238. *Phys. Rev.* **4(5)**, 1889-1906 (1971).
903
904 81. Hiess, J., Condon, D. J., McLean, N., & Noble, S. R. U-238/U-235 Systematics in Terrestrial Uranium-Bearing Minerals.
905 *Science* **335(6076)**, 1610-1614 (2012). <https://doi.org/10.1126/science.1215507>
906
907 82. Cheng, H. Edwards, R. L. Hoff, J. *et al.* The half-lives of uranium-234 and thorium-230. *Chem. Geol.* **169(1-2)**, 17-33 (2000).
908 [https://doi.org/10.1016/S0009-2541\(99\)00157-6](https://doi.org/10.1016/S0009-2541(99)00157-6)
909
910 83. Schärer, U. The effect of initial ²³⁰Th disequilibrium on young U-Pb ages: the Makalu case, Himalaya. *Earth. Planet. Sci.*
911 *Lett.* **67**, 191-204 (1984).
912
913 84. Rubatto, D. & Hermann, J. Experimental zircon/melt and zircon/garnet trace element partitioning and implications for the
914 geochronology of crustal rocks. *Chem. Geol.* **241**, 38–61 (2007). <https://doi.org/10.1016/j.chemgeo.2007.01.027>
915
916 85. Smoliar, M. I., Walker, R. J., & Morgan, J. W. Re-Os ages of group IIA, IIIA, IVA, and IVB iron meteorites. *Science* **271**,
917 1099–1102 (1996).
918
919 86. Selby, D., Creaser, R. A., Stein, H. J. *et al.* Assessment of the ¹⁸⁷Re decay constant by cross calibration of Re–Os
920 molybdenite and U–Pb zircon chronometers in magmatic ore systems. *Geochim. Cosmochim. Acta.* **71(8)**, 1999-2013
921 (2007). <https://doi.org/10.1016/j.gca.2007.01.008>
922
923 87. Schoene, B., Latkoczy, C., Schaltegger, U. & Günther, D. A new method integrating high-precision U-Pb geochronology
924 with zircon trace element analysis (U-Pb TIMS-TEA). *Geochim. Cosmochim. Acta.* **74(24)**, 7144-7159 (2010).
925 <https://doi.org/10.1016/j.gca.2010.09.016>
926
927 88. Nowell, G.M. & Parrish, R.R. Simultaneous acquisition of isotope compositions and parent/daughter ratios by non-isotope
928 dilution-mode plasma ionisation multi-collector mass spectrometry (PIMMS). In Plasma Source Mass Spectrometry: The
929 New Millennium (Holland, G. & Tanner, S.D. eds) *Royal Soc. Chem., Spec. Publ.* **267**, 298-310 (2001).
930
931 89. Lawley, C. J. M. & Selby, D. Re-Os Geochronology of Quartz Enclosed Ultra-fine Molybdenite: Implications for Ore
932 Geochronology. *Econ. Geol.* **107(7)**, 1499-1506 (2012). <https://doi.org/10.2113/econgeo.107.7.1499>
933
934 90. Selby, D. & Creaser, R. A. Macroscale NTIMS and microscale LA-MC-ICP-MS Re-Os isotopic analysis of molybdenite:
935 Testing spatial restrictions for reliable Re-Os age determinations, and implications for the decoupling of Re and Os within
936 molybdenite. *Geochim. Cosmochim. Acta.* **68**, 3897-3908 (2004). <https://doi.org/10.1016/j.gca.2004.03.022>

937
938
939
940
941
942
943
944
945
946
947
948

91. Li, Y., Selby, D., Condon, D. & Tapster, S. Cyclic magmatic-hydrothermal evolution in porphyry systems: High-precision U-Pb and Re-Os geochronology constraints from the Tibetan Qulong porphyry Cu-Mo deposit. *Econ. Geol.* **112(6)**, 1419-1440 (2017). <https://doi.org/10.5382/econgeo.2017.4515>
92. Markey, R., Stein, H. J., Hannah, J. L. *et al.* Standardizing Re-Os geochronology: A new molybdenite reference material (Henderson, USA) and the stoichiometry of Os salts. *Chem. Geol.* **244**, 74–87 (2007).
93. Zimmerman, A., Stein, H. J., Morgan, J. W., Markey, R. J., & Watanabe, Y. Re-Os geochronology of the El Salvador porphyry Cu-Mo deposit, Chile: Tracking analytical improvements in accuracy and precision over the past decade. *Geochim. Cosmochim. Acta.* **131**, 13–32 (2014).

949 **Supplementary Data**

950 1/ Zircon U-Pb CA-ID-TIMS and molybdenite Re-Os geochronology data

951 2/ Whole-rock XRF & ICP-MS geochemistry data

952 3/ Zircon LA-ICP-MS data

953 4/ Zircon Lu-Hf isotope data

954

Figures

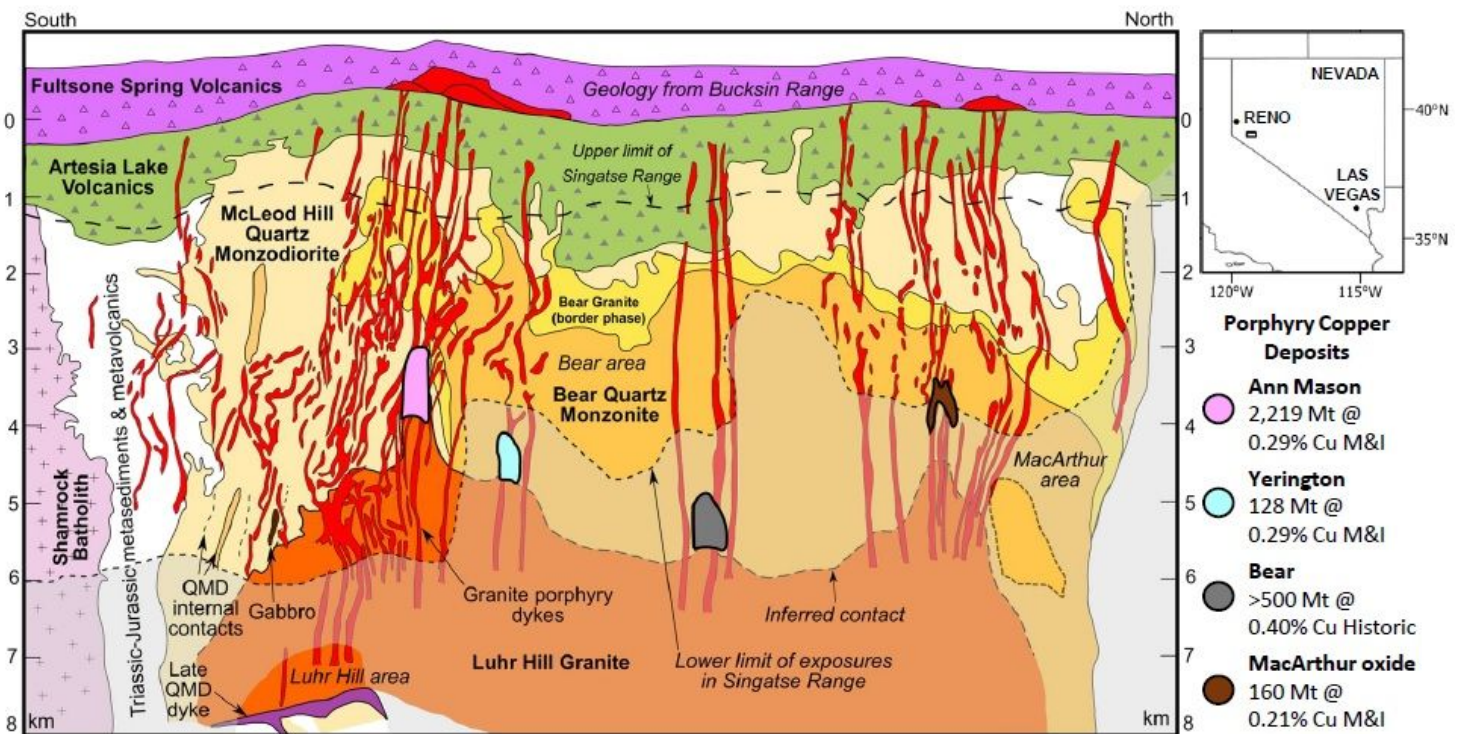


Figure 1

Pre tilt cross section through the Yerington District, Nevada Reconstructed to a palaeo depth of 8 km, showing the intrusive units of the Jurassic Yerington batholith, the various generations of porphyry dyke swarms which were emplaced through apophyses of the Luhr Hill granite, the district's four known porphyry copper deposits and overlying volcanics (Yerington and Bear deposits projected onto section) QMD quartz monzodiorite Modified after 27 31 32 Resource estimates from 35 37 39 M&I measured indicated historic non compliant historic estimate

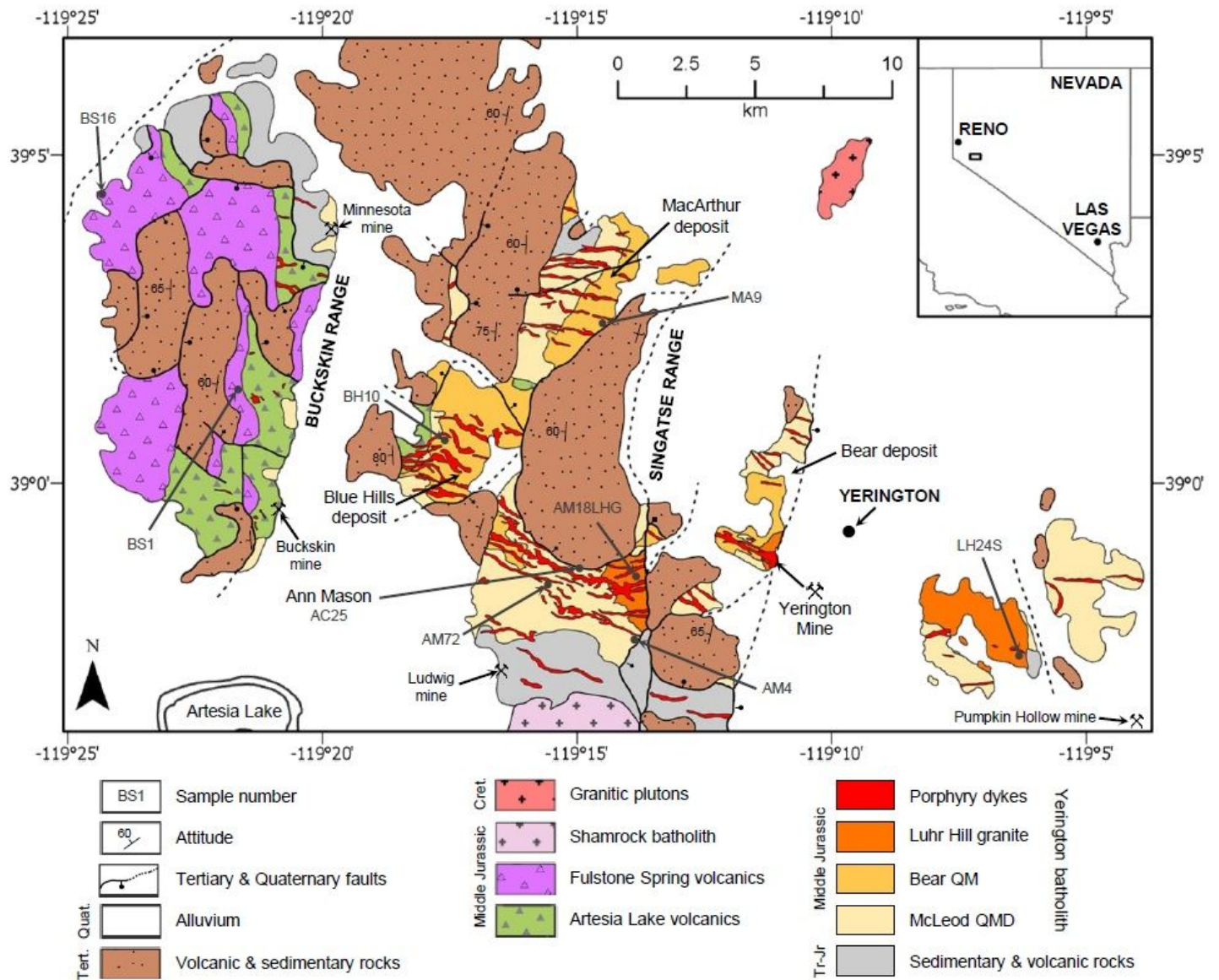


Figure 2

Simplified geological map of the Yerington District, Nevada annotated with known major mineral deposits and localities sampled for zircon U Pb CA ID TIMS geochronology (Fig 4 Geology is modified from 34 67 68 QM quartz monzonite, QMD quartz monzodiorite WGS 1984

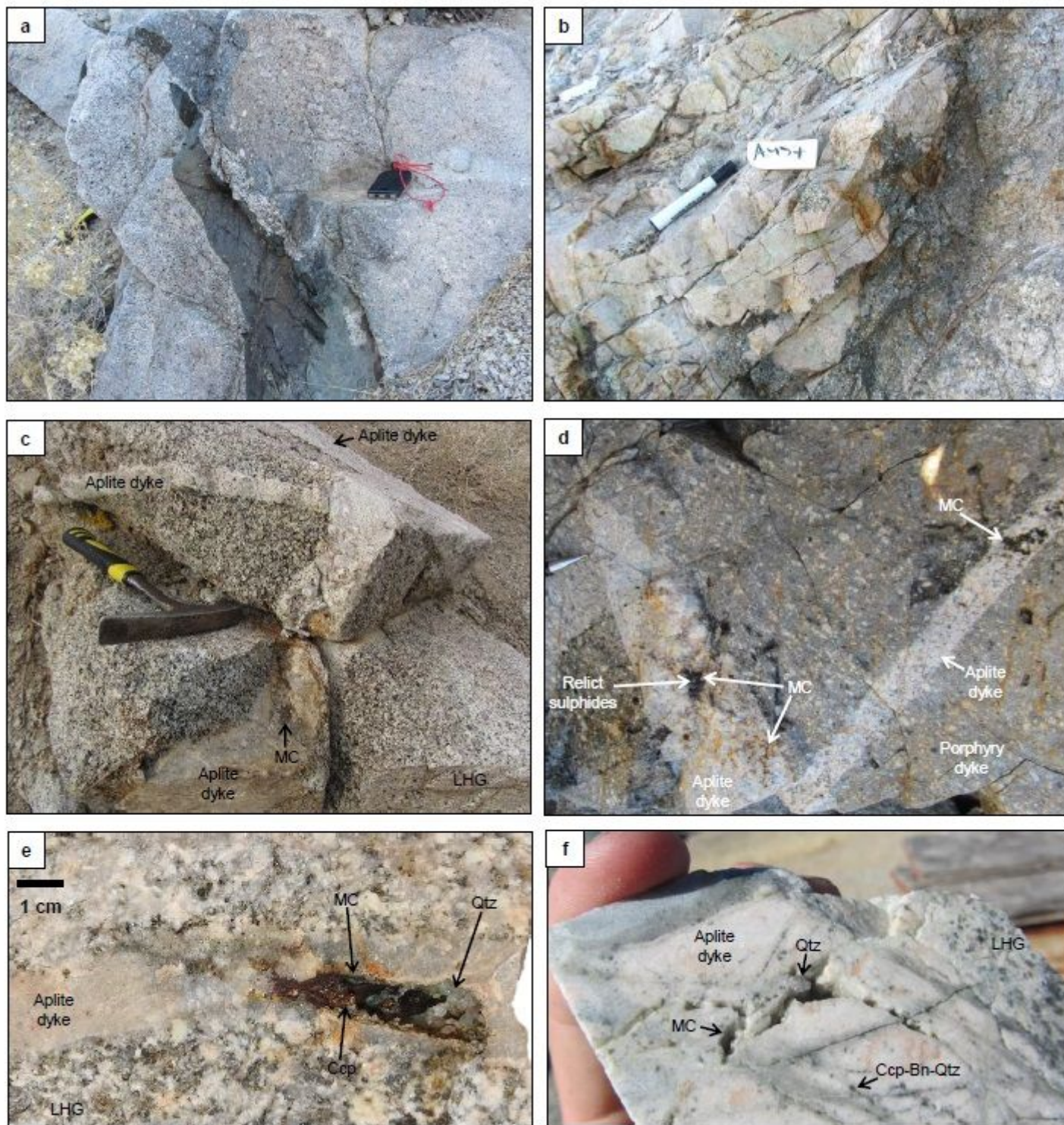


Figure 3

Temporal relations in the Yerington magmatic system Field photographs of a cross cutting relations of multiple porphyry dyke generations which cut the LHG cupola b lobate contacts and evidence for mingling of co eval magmas between an aplite dyke and porphyry dyke Secondary copper staining prevalent in the aplite dyke c d, multiple generations of aplite dykes hosting pegmatitic segregations and mineralised miarolitic cavities (MC The aplite dykes sharply cross cut the cupola zone of the LHG and a

porphyry dyke Both the aplite and porphyry dykes lie palaeo vertically beneath the Ann Mason porphyry deposit e, cupola zone of LHG cut by an aplite dyke hosting a chalcopyrite (mineralised miarolitic cavity Qtz quartz f, drill core from the Ann Mason porphyry deposit showing LHG cut by an aplite dyke hosting miarolitic cavities and early chalcopyrite bornite quartz (Ccp Bn Qtz) A type, nomenclature after 44 veins, which locally truncate at the dyke's margin B, e f after 32

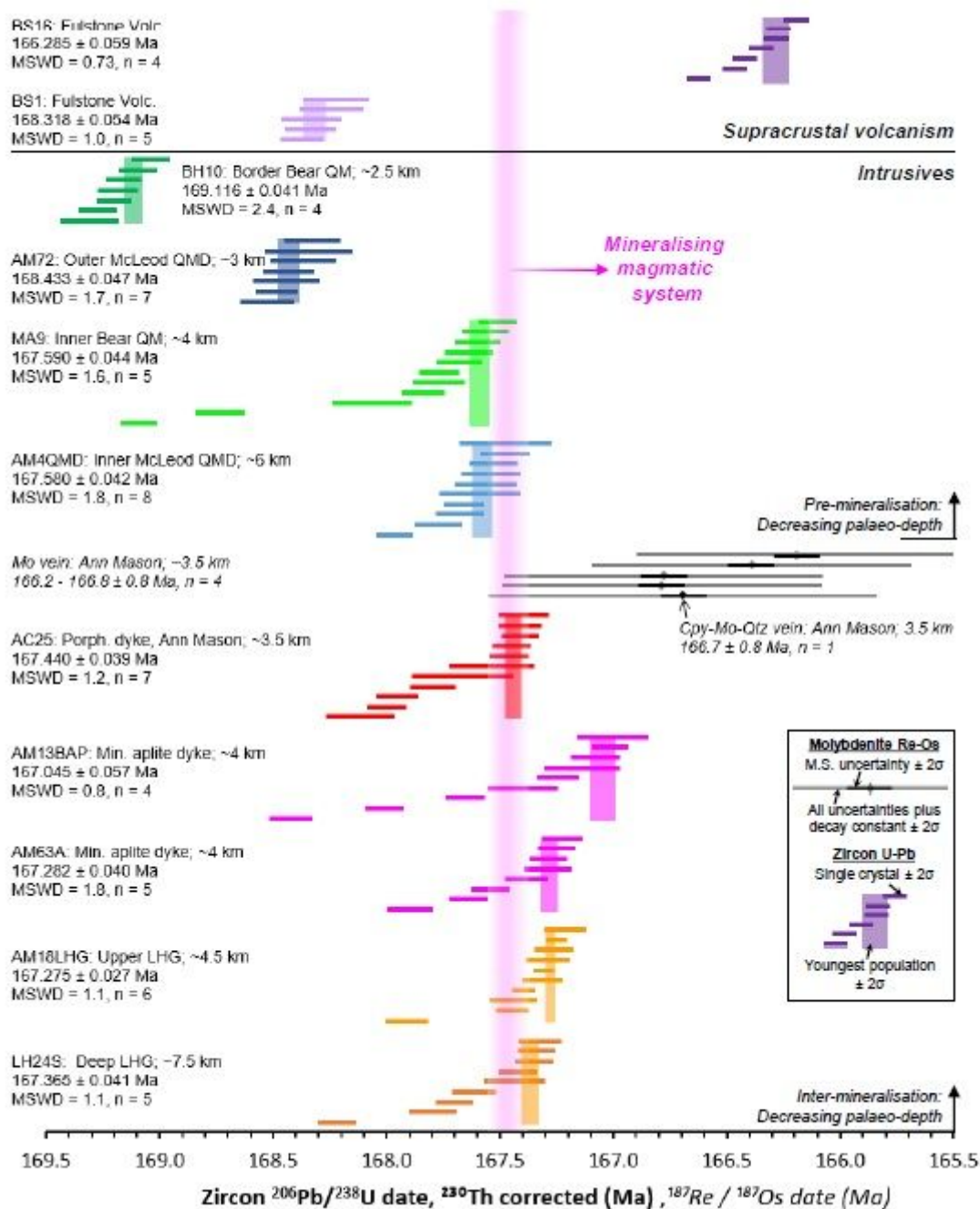


Figure 4

Geochronological framework for the Yerington porphyry system Zircon single grain U Pb CA ID TIMS and molybdenite Re Os geochronological framework for samples spanning the Yerington magmatic system

Pre and inter mineralisation intrusive samples grouped and plotted in order of approximate palaeo depth
 27 Sample details in S supplementary Data 1 We take the weighted mean of the youngest population of zircon dates that formed a statistically acceptable Mean Square Weighted Deviation (or chi squared) as the best approximation for the crystallisation of the host magma Porph porphyry M S mass spectrometry Error bars at 2 σ

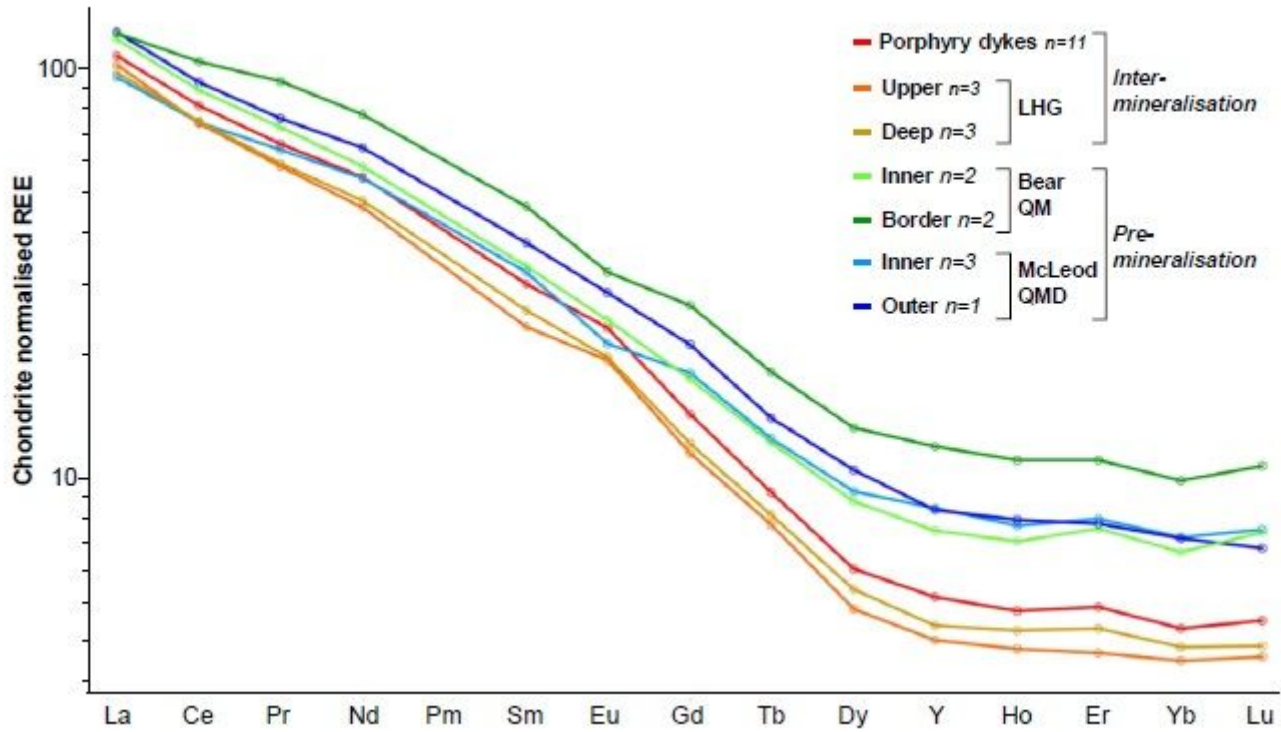


Figure 5

Chondrite normalised 69 mean whole rock REE plots LHG and porphyry dykes are distinct from the Bear QM and McLeod QMD intrusions, having slightly positive Eu anomalies and steeper MREE/HREE curves

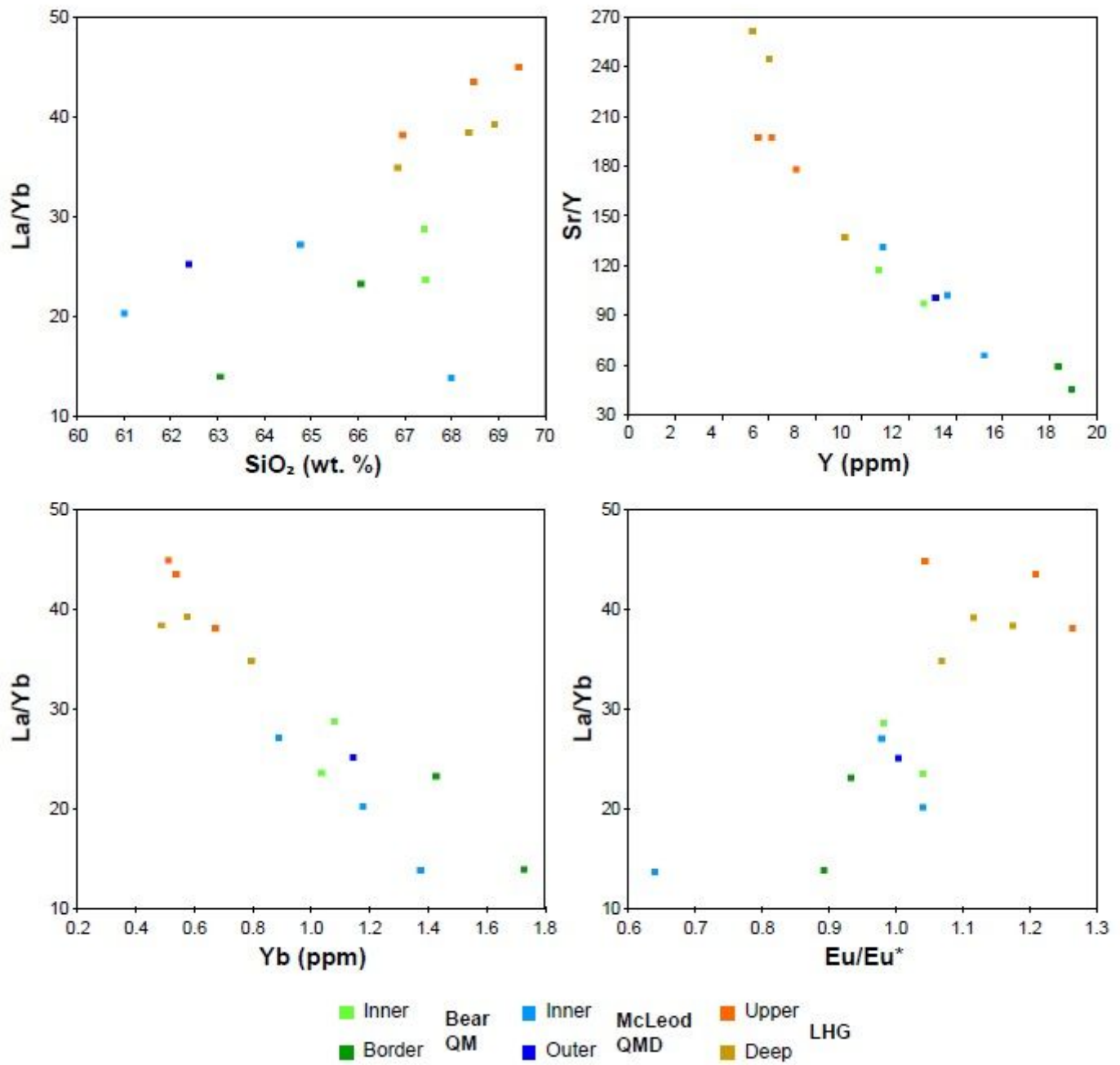


Figure 6

Whole rock geochemical compositions of plutonic units in the Yerington magmatic system. Major elements in part overlap between the mineralogically distinct 27 intrusive units. Distinct differences between pre mineralisation (Bear QM and McLeod QMD) and inter mineralisation (units are seen in trace element ratios).

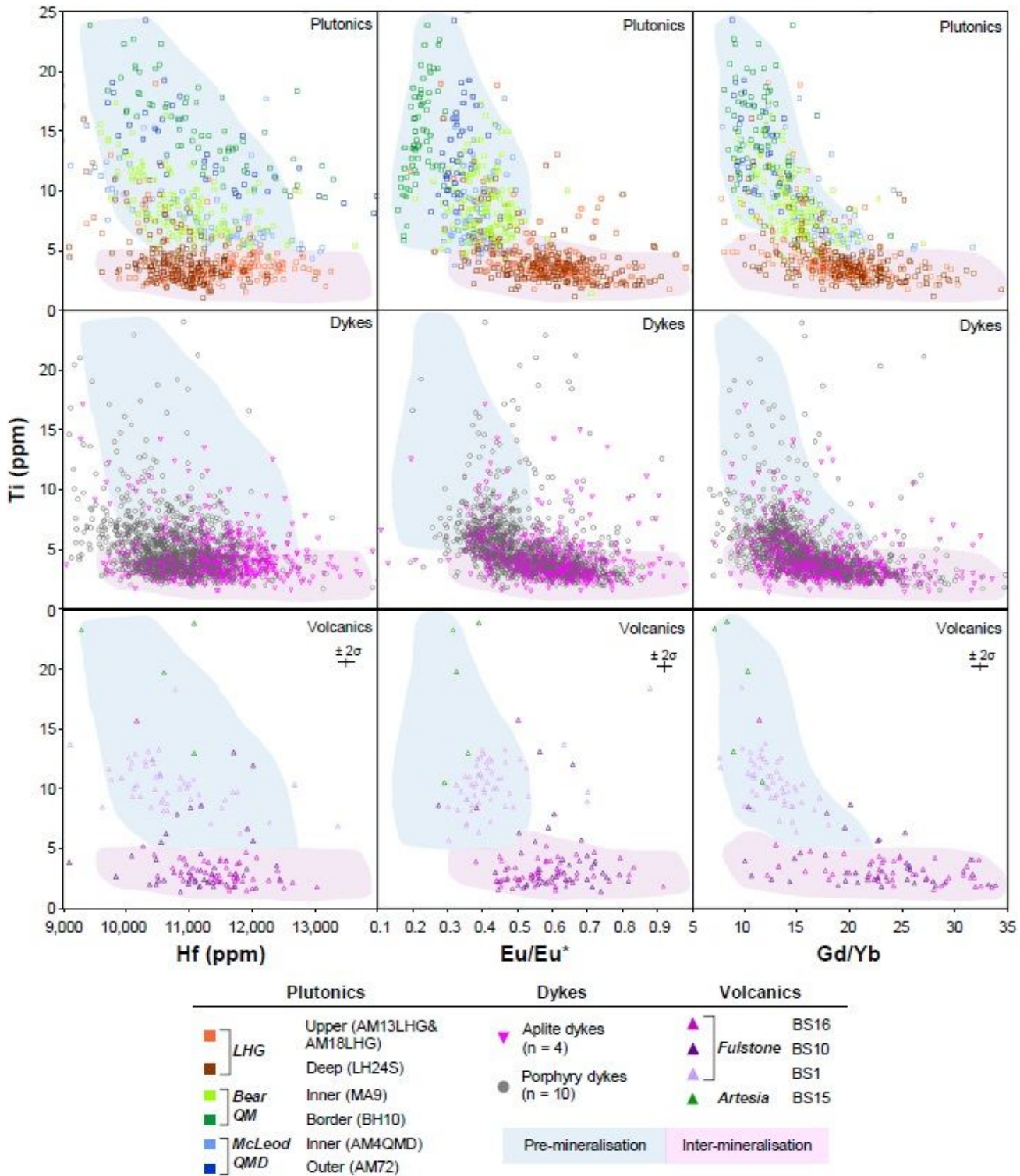


Figure 7

Zircon trace element signatures through the Yerington porphyry system Zircon LA ICP MS trace element data from samples spanning, temporally and spatially, the Yerington porphyry system ..'Pre mineralisation' and 'inter mineralisation' fields shaded Only zircon rim data have been plotted See Fig S 7 10 for full sample breakdown along with zircon core data

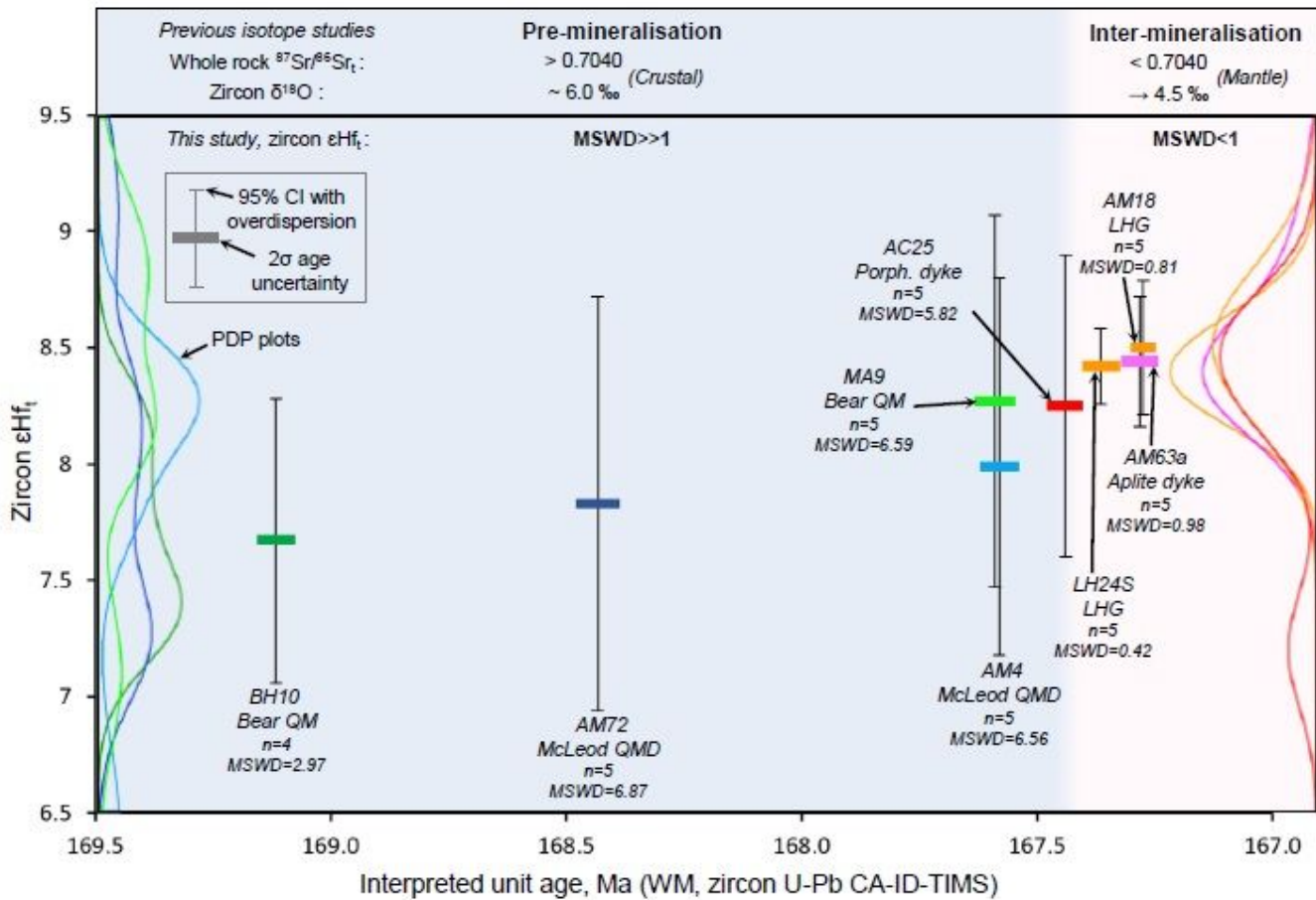


Figure 8

Zircon ϵHf_t through the Yerington porphyry system Time corrected zircon ϵHf_t versus interpreted zircon age for samples spanning the Yerington porphyry system Age determinations for each sample are weighted mean (from zircon single grain U Pb CA ID TIMS analyses, with error bars at 2 σ (Fig 4 ϵHf_t error bars at 95 confidence interval (with overdispersion ..'Pre and 'inter mineralisation' fields shaded Probability density plots (inset, coloured as per sample From the MSWD data for ϵHf_t „pre mineralisation' units show over dispersion (MSWD > 1 and 'inter mineralisation' units show under dispersion (MSWD < 1 Data compared to previous whole rock $^{87}\text{Sr}/^{86}\text{Sr}_t$ and zircon $\delta^{18}\text{O}$ isotope studies, which show subtle shifts from crustal to mantle isotopic signatures 57 59

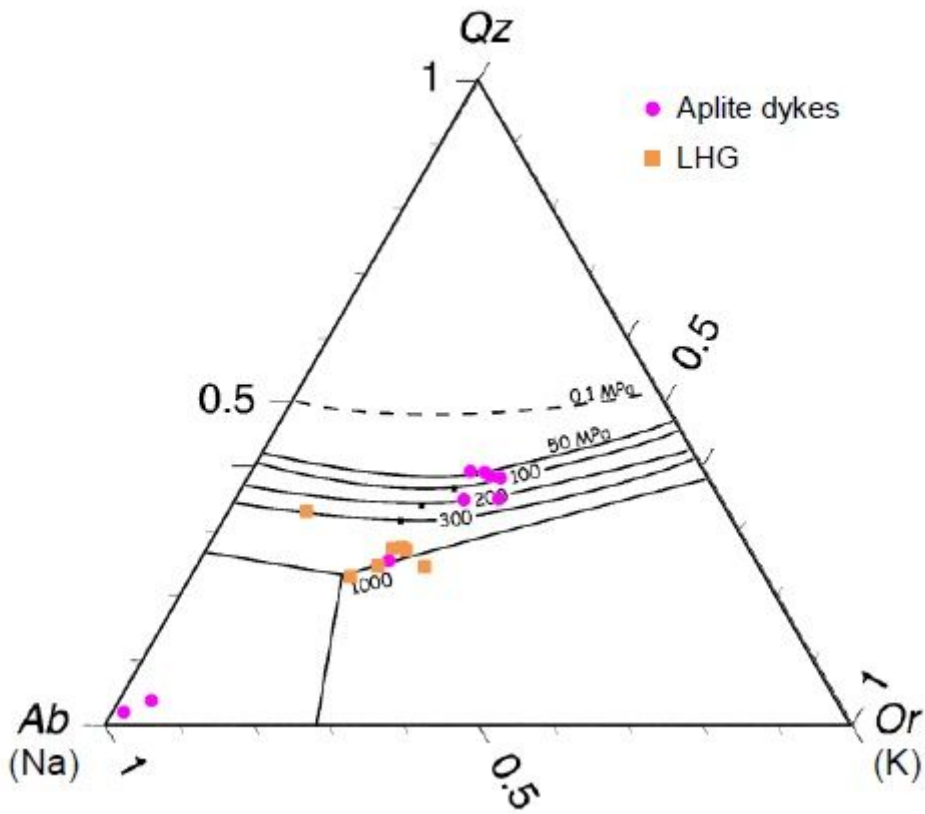


Figure 9

Depth of different magma sources CIPW normative mineralogy (method of 70 from whole rock XRF data for LHG and aplite dykes plotted on the H₂O saturated haplogranitic melt minima plot 61 Cotectic lines and eutectics are a function of pressure and therefore the whole rock data can be used to provide constraints for the pressure of magma differentiation 54 from which depth can be approximated Other units plotted in Fig S 11

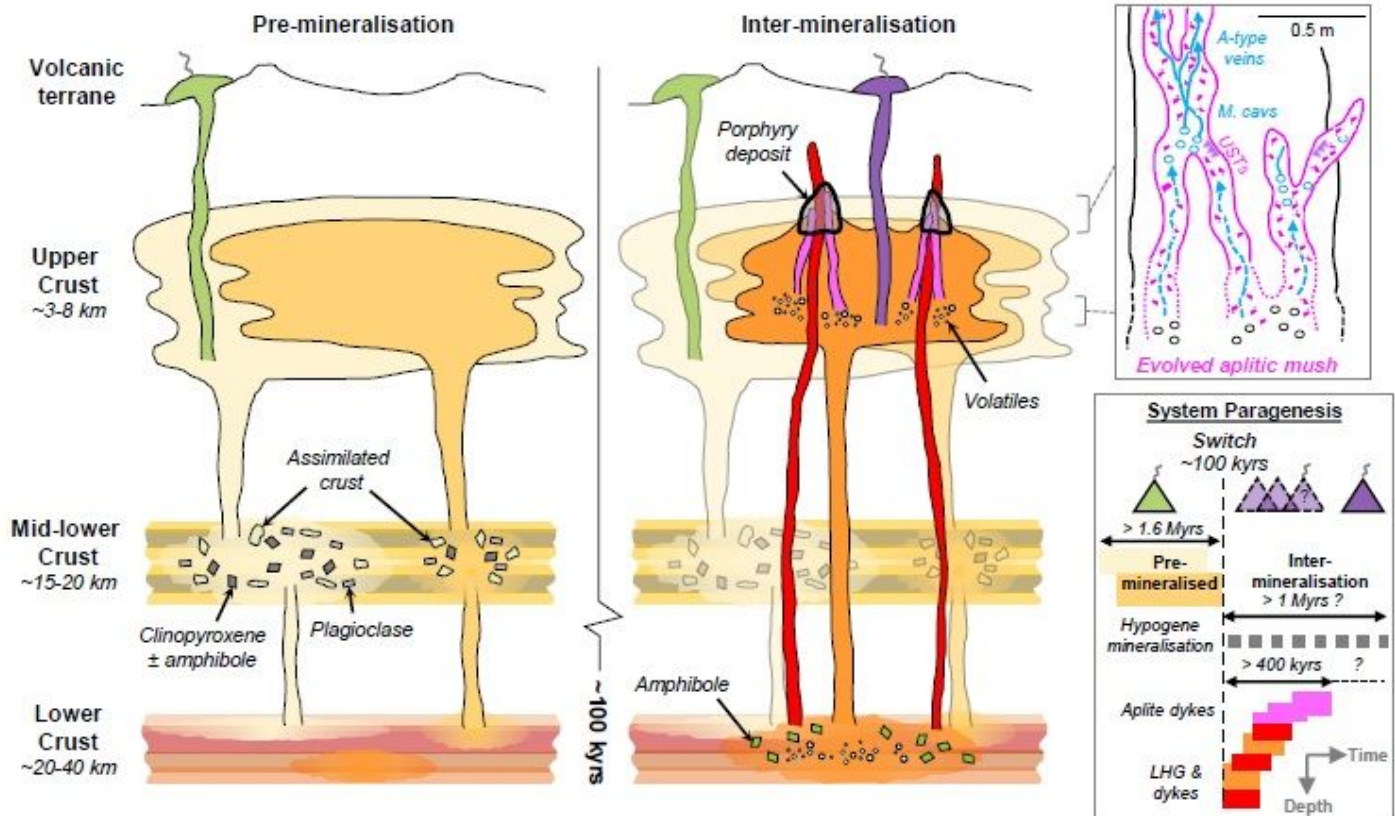


Figure 10

A rapid switch in magmatic plumbing to tap porphyry mineralising magmas Simplified system paragenesis and conceptual cross section through the porphyry system A long lived (1.6 Myrs) evolution and contemporaneous emplacement of precursor plutonics, with volcanic activity, was followed by a rapid (100 kyrs) switch in magmatic plumbing to tap fertile porphyry deposit forming magmas from a 20-40 km deep lower crustal staging ground where they predominately underwent amphibole dominated fractional crystallisation From this zone of melt evolution, fertile magmas were emplaced into the shallow crust to form plutons and porphyry stocks, and underwent further differentiation at 3-8 km depth, with episodic upward injection of multiple generations of aplite dykes for 400 kyrs, which acted as crystal mush conduits for mineralising fluids As mineralising fluids exploited these conduits, porphyry deposit formation continued episodically for potentially in excess of 1 Myrs, and may have been coeval with volcanism M.cavs miarolitic cavities USTs unidirectional solidification textures Vein nomenclature after 44 Modified after 5, 32, 54

Supplementary Files

This is a list of supplementary files associated with this preprint. Click to download.

- [CarteretalSupplementaryData1ZirconUPbandmolybdeniteReOsgeochronology.xlsx](#)

- [CarteretalSupplementaryData2WholerockXRFXICPMSgeochemistry.xlsx](#)
- [CarteretalSupplementaryData3ZirconLAICPMSdata.xlsx](#)
- [CarteretalSupplementaryData4ZirconLuHfisotopedata.xlsx](#)
- [CarteretalSupplementaryFigures.pdf](#)